UNIVERSITY OF CAMBRIDGE

Flow Characteristics, Setting, and Basal Boundary Condition of North Greenland Outlet Glaciers

Thomas Perry

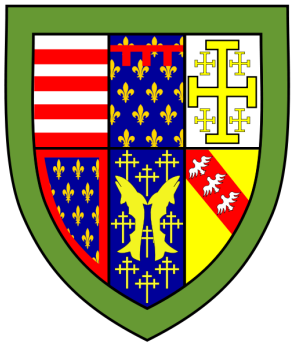

Queens' College

Thesis submitted 12th June 2014 for the degree of Master of Philosophy

Abstract

Temporal variability in the partitioning of mass loss from the Greenland Ice Sheet suggests a complex response to recent climatic change. The contribution to sea level rise from tidewater glaciers is also spatially variable across the ice sheet, and observations reveal their contrasting behaviour at a regional scale. Whilst ice-ocean interaction may explain their dynamics in the south of Greenland, the warm subtropical waters responsible for this extend only to mid-latitudes. In this study, the geometric setting and bed condition is therefore investigated to better understand the flow characteristics and dynamics of high-latitude tidewater glaciers in Greenland. New ice thickness measurements are combined with a novel mass conservation method to reconstruct high resolution (<300 m) bed topographies for 4 tidewater glaciers in northern Greenland. A 3D inversion using control methods is then applied to each glacier with the full-stokes model, Elmer/Ice, to calculate basal drag. The bed topographies reveal that these glaciers are underlain by deeply incised channels, which extend more inland and descend further below present sea level than previously thought. The results of the inversions show spatially variable drag across the beds of these glaciers, but highlight a close relationship with local changes in bed elevation. This may be attributed to form drag by topographic highs, or the infilling of depressions with soft sediment and water. Regardless, the results of this study imply that these glaciers are far more vulnerable to future sea level rise than previously recognised, and may themselves contribute significantly to this in response to a relatively small, future perturbation.

Acknowledgements

I am especially grateful to a number of people, without whom this project would not have been possible. First and foremost, I thank my supervisor, Poul Christoffersen, for his invaluable guidance and support over the last year. I am also particularly grateful to Joe Todd for answering my endless questions regarding the Elmer/Ice model, and to Toby Beham who kindly provided the GrOGG flight data used in this project.

Financially, this year would not have been possible without the support of my parents, and I am indebted to them (quite literally) for their enthusiasm for my time here. Last but certainly not least, I thank all my colleagues, the 'sports fans', on this MPhil course and my friends in Queens' for some unforgettable experiences and for keeping me sane when the going got tough.

Contents

List of Figures

List of Tables

Nomenclature

α	Power formulation of β
$\bar{u_n}$	Average velocity component normal to bed slope
$\bar{u}$	Mean velocity across flowline transect
β	Slip coefficient
$\dot{\epsilon}$	Shear strain rate
$\dot{b}$	Net mass balance
η_i	Effective viscosity of ice
$\hat{H}$	Ice-equivalent thickness
λ	Regularisation term
μ	Coefficient of friction
ρ_i	Density of ice
ρ_w	Density of sea water
σ_n	Compressive normal stress
τ_*	Residual strength
τ_b	Basal shear stress
τ_d	Driving stress
τ_f	Frictional stress
θ_c	Angle between bed obstacle and bed slope
θ_s	Slope of the ice surface

φ	Internal friction angle
A	Ice softness parameter
A_0	Ice softness prefactor
b_{sfc}	Surface mass balance
C	Debris concentration
c_0	Apparent cohesion
g	Gravity
H	Ice thickness
h_w	Sea surface elevation
J_0	Initial cost function
J_{reg}	Regularised cost function
J_{tot}	Total cost function
n	Creep exponent
N_p	Effective pressure
N_s	Effective normal stress
P_i	Ice overburden pressure
P_w	Subglacial water pressure
q	Ice flux
Q^*	Activation energy for ice creep
q_{out}	Ice flux from fluxgate
R	Gas constant
t	Time
T_0	Melting point of ice at 1 atm
T_i	Ice temperature

u_{ctr}	Centreline velocity
u_{sfc}	Surface ice velocity
u_{ss}	Soft bed sliding velocity
W_f	Local flowline width
z_x	Depth below sea level

Chapter 1

Introduction

The glacial and interglacial cycles within Earth's climate record have historically driven the growth and decay of large ice masses in multiple settings. Today, ice is mostly confined to the poles as three major ice sheets that collectively contain some 65 m of potential sea level rise [Vaughan et al., 2013]. The Greenland Ice Sheet in the Northern Hemisphere represents just 13% of this, yet currently contributes almost twice as much ice to the oceans as Antarctica [Shepherd et al., 2012; Bamber et al., 2013]. These losses are partitioned between surface runoff from melting, and efficient iceberg calving at marine-terminating outlet glaciers, however their relative contribution in the long-term is uncertain. Nearly a decade ago, iceberg calving accounted for two thirds of Greenland's contribution to sea level rise [Rignot and Kanagaratnam, 2006], yet the latest estimates now suggest that surface runoff is dominant [Enderlin et al., 2014]. This temporal variability therefore represents an important component in future predictions of Greenland's contribution to sea level rise. Recent appraisals view the role of runoff and surface mass balance with high confidence [Vaughan et al., 2013], yet comparatively little is known about outlet glaciers terminating in tidewater, henceforth referred to as tidewater glaciers, and as such these form the focus of this study. Numerous tidewater glaciers fringe the margins of the Greenland Ice Sheet and are characterised by discrete zones of fast-flow (>1000 m yr^{-1}) that drain ice from the interior. In recent decades, research has revealed the near-synchronous dynamic thinning and acceleration of multiple tidewater glaciers in Greenland [e.g. Krabill et al., 2004; Pritchard et al., 2009], which has accelerated their contribution to sea level rise and fundamentally altered the velocity structure of the ice sheet [Rignot and Kanagaratnam, 2006; Rignot et al., 2011]; changes which may have important implications for its long-term stability. Understanding these fast-flow systems is

therefore an important issue in contemporary glaciology.

An obvious focus has been on the drivers behind this fast ice flow, and their sensitivity to 21st century climate projections. At mid to southerly latitudes in Greenland, some of the high velocities observed on tidewater glaciers such as Kangerdlugssuaq Glacier in the southeast have been attributed to the interaction of ice with the ocean [Christoffersen et al., 2012]. In particular, warm subsurface waters sourced from the subtropics have been detected in a number of fjords [e.g. Holland et al., 2008; Rignot et al., 2010], and these warm and saline waters have been shown to interact with cold and fresh subglacial meltwater discharged across the grounding lines of tidewater glaciers, producing vigorous melting at ice fronts through forced convection. It is speculated that this ice-ocean interaction enhances calving through undercutting [O'Leary and Christoffersen, 2013], which in turn reduces the backstress on ice upstream. However, hydrographic surveys and analyses of interannual terminus stability show that these waters do not appear to reach latitudes higher than about 69°N [Seale et al., 2011]. Despite this, flow velocities and ice discharge remain high in northern Greenland [van den Broeke et al., 2009], which suggests that different components may control ice flow in this sector.

A review of glacier velocities by Moon et al. [2012] demonstrated contrasting behaviour of neighbouring glaciers at a regional scale, and this complex behaviour may stem from differences in the geometric setting and basal condition of these glaciers. It is possible that in the absence of a strong marine perturbation, which has been shown to heavily influence glacier dynamics further south [Nick et al., 2009], the role of runoff and its drainage to the bed [Zwally et al., 2002] could play a far more important role in governing ice dynamics at high latitudes in Greenland. Specifically, the high diurnal temperature ranges in the north of Greenland combined with projections of future warming and increased runoff improve the efficacy of surface melt-induced acceleration [Steffen and Box, 2001; Schoof, 2010]. At present however, the condition of the bed remains a poorly constrained parameter that constitutes an important foundation for prognostic investigations into future change.

Very little is known about the bed condition of high latitude tidewater glaciers in Greenland. This is in part due to their remoteness, the limited availability of quantitative data in these regions, and the obvious difficulties and costs associated

with measuring or observing the bed directly. Fortunately, a proliferation in the number of airborne geophysical survey campaigns over Greenland and a recent emphasis on acquiring data over fast-flowing tidewater glaciers [Bamber et al., 2013], now means that bed topographies can be derived with greater accuracy and at higher resolutions than previously possible. In addition, advances in computational power now permit detailed assessments of the bed using more complex numerical models, already powerful tools in glaciology.

The aim of this study is to therefore utilise these recent advances to assess conditions at the bed of several tidewater glaciers in northern Greenland in order to understand their flow characteristics in more detail. In this regard, there are two key research objectives for this study:

1. To derive robust, high-resolution basal geometries of selected tidewater glaciers in northern Greenland

2. To calculate and evaluate the role of basal drag in influencing the flow of these glaciers

The specific glaciers analysed in this research are presented in Chapter 2. Chapter 3 reviews ice dynamic processes and those particularly relevant to fast-flowing tidewater glaciers. The datasets used, procedure for deriving bed geometries, and the 3D model is then examined in Chapter 4. Results are presented in Chapter 5 and discussed in further detail in Chapter 6.

Chapter 2

Study Area

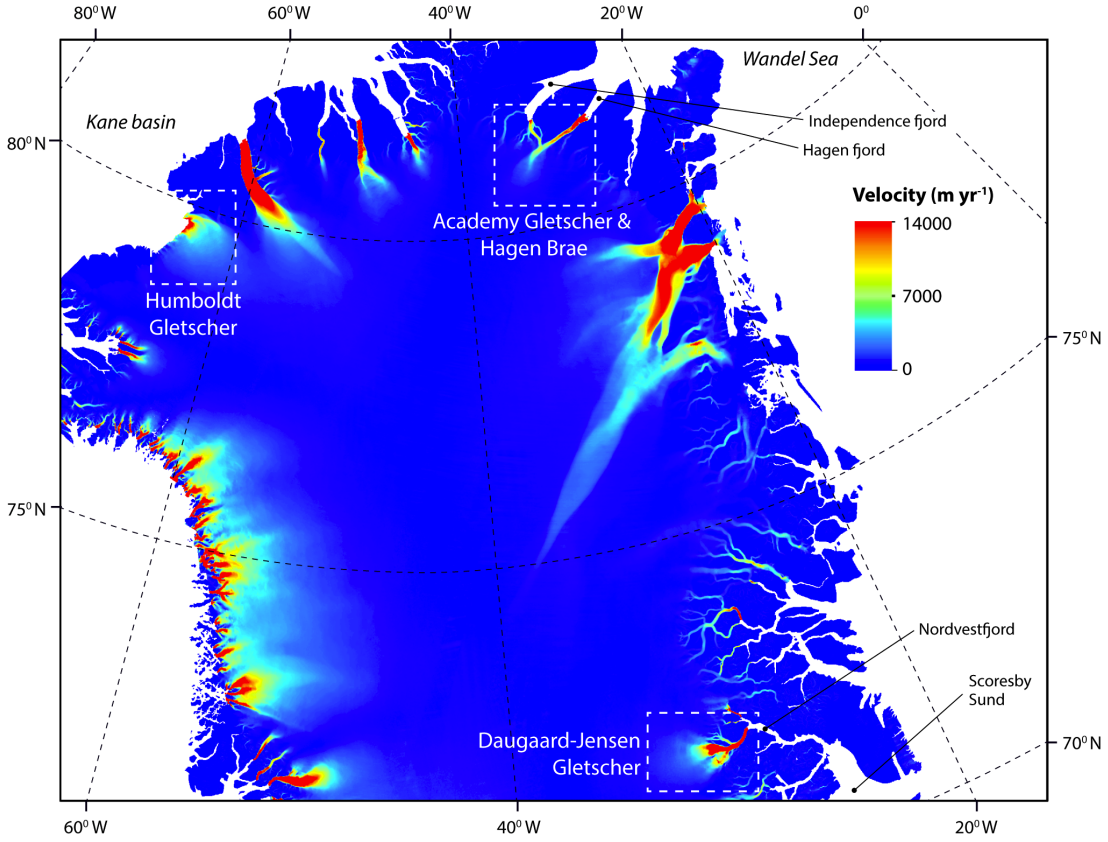

Figure 2.1: Map of study area illustrating locations of glaciers analysed in this research (white dashed boxes). Placenames referred to in the text are also labelled. Annotations are overlaid on a composite velocity map from the MEaSUREs dataset

This study focuses on four tidewater outlet glaciers located in northern Greenland (Fig. 2.1): Daugaard-Jensen Gletscher (71°50'N), Hagen Brae (81°35'N), Academy Gletscher (81°45'N) and Humboldt Gletscher (79°40'N). Collectively, the drainage areas of these glaciers constitutes a notable portion of the ice sheet and together

they discharge some 17.2 km^3 of ice to the oceans every year [Rignot and Kanagaratnam, 2006]. Whilst they exhibit fast flow however, they have been shown to be more or less in balance and stable in recent years, and therefore the snapshots of their velocities used in later analysis are especially representative of their general flow characteristics. By assessing these glaciers, there is the opportunity to identify essential features of the basal boundary condition for a large portion of the ice sheet isolated from strong ocean forcing. These glaciers have previously received little attention compared to others such as Petermann Glacier [Nick et al., 2010] or 79north Glacier [Seroussi et al., 2011], but recent airborne surveys now permit detailed analysis. The setting and characteristics of each glaciers are now reviewed in the following sections.

2.1 Daugaard-Jensen Gletscher

In East Greenland, Daugaard-Jensen Gletscher descends steeply from the ice sheet where ice accelerates to speeds of up to 4 km yr^{-1} whilst being steered through mountainous topography, before terminating in Nordvestfjord, a northern tributary to the main Scoresby Sund fjord system [Walsh et al., 2012]. The glacier drains 4% of the ice sheet, an area of some 50,000 km^2, and annually discharges 10 km^3 of ice to the oceans [Rignot and Kanagaratnam, 2006]. This represents 3-4% of the total calving flux from the Greenland Ice Sheet, and as such it is regarded as one of the most productive glaciers in East Greenland [Dowdeswell et al., 1992]. Despite this, various studies have shown the glacier to be in balance and stable [Stearns et al., 2005; Bevan et al., 2012]. Estimates of its mass balance (Fig. 2.3) suggest up 20 cm yr^{-1} of accumulation inland and up to 25 cm yr^{-1} of melting near the terminus [Box et al., 2006]. A small floating ice tongue extends several kilometres in front of the grounding line with an estimated terminus thickness of 500 m based on iceberg overturning [Reeh and Olesen, 1986], however widening and deepening of the fjord likely inhibits any further advance [Reeh et al., 1999]. Importantly, velocity fluctuations and the detection of numerous glacial earthquakes, which typically arise from a brief (30-60s) but substantial sudden movement of ice (10 km^3), suggest a complex bed and a dynamic subglacial hydrological system [Reeh and Olesen, 1986; Ekström et al., 2006]. In places, bright radar echoes also suggest the presence of basal meltwater [Layberry and Bamber, 2001], consistent with estimates of a regional geothermal heat flux of $\sim$ 75 mW m^{-2} (Fig. 2.2) [Greve, 2005].

2.2 Academy Gletscher & Hagen Brae

Dramatic coastal relief also affects ice flow in the northeast of Greenland, where Academy Gletscher and Hagen Brae are again steered through mountainous terrain where they then terminate in Independence and Hagen fjord respectively. Together, they drain approximately 32,300 km^2 of the ice sheet, discharging 3.5 km^3 yr^{-1} into the Wandel Sea [Rignot and Kanagaratnam, 2006], where terminus velocities reach approximately 600 m yr^{-1} for both glaciers [Joughin et al., 2010]. Their flow regimes have been debated as observations note densely packed icebergs and sikussak in both fjords, suggesting either prolonged stability or recent retreat [Davies and Krinsley, 1962]. Recent investigations advocate the latter when compared to historical records [e.g. Higgins, 1991], as Interferometric Synthetic Aperture Radar (InSAR) evidence reveals acceleration of both glaciers by up to 400 m yr^{-1} and thinning by up to 4 m yr^{-1} since the late 1990s [Rignot et al., 1997; Abdalati et al., 2001; Joughin et al., 2010]. Satellite imagery also shows the retreat of the terminus of Hagen Brae off a small pinning point in the fjord, which may have aided its speedup [Rignot et al., 2001]. Whilst both glaciers are mostly in balance [Rignot and Kanagaratnam, 2006], thinning estimates are supported by modelled surface mass balance (Fig. 2.3), which predicts up to 25 cm yr^{-1} of accumulation in the interior but up to 100 m yr^{-1} of ablation near their termini [Box et al., 2006]. This may be further supplemented by a moderate geothermal heat flux of $\sim$ 75 mW m^{-2} (Fig. 2.2) [Greve, 2005]. Since Academy Gletscher and Hagen Brae share the same inland catchment area and the same equilibrium line altitude (ELA) [Rignot et al., 2001], they are treated together from hereon.

2.3 Humboldt Gletscher

The widest calving front in Greenland is that of Humboldt Gletscher, located in the northwest. Its terminus spans some 90 km, draining 47,300 km^2 of the ice sheet but discharging just 3.7 km^3 yr^{-1} into the Kane basin [Rignot and Kanagaratnam, 2006]. Velocities are spatially variable across the front, with the fastest (up to 500 m yr^{-1}) confined to the northeastern margin, consistent with the location of a deep subglacial trough [Joughin et al., 1999, 2010]. It is this area where calving is most frequent [Bindschadler et al., 1987], where a small floating section is located, and where recent retreat has been observed [Box and Decker, 2011]. Losses here however, are partially offset by higher accumulation near the glacier's

southwestern margin, which is close to equilibrium [Rignot et al., 2001; Rignot and Kanagaratnam, 2006]. Additional surface mass balance data shows a maximum accumulation of 15 cm yr^{-1} (Fig. 2.3), which agrees with ice core data that shows an average accumulation of 14 cm yr^{-1} [Anklin et al., 1998]. Humboldt Gletscher has the lowest geothermal heat flux of the glaciers studied here (Fig. 2.2), at $\sim$ 60 mW m^{-2} [Greve, 2005].

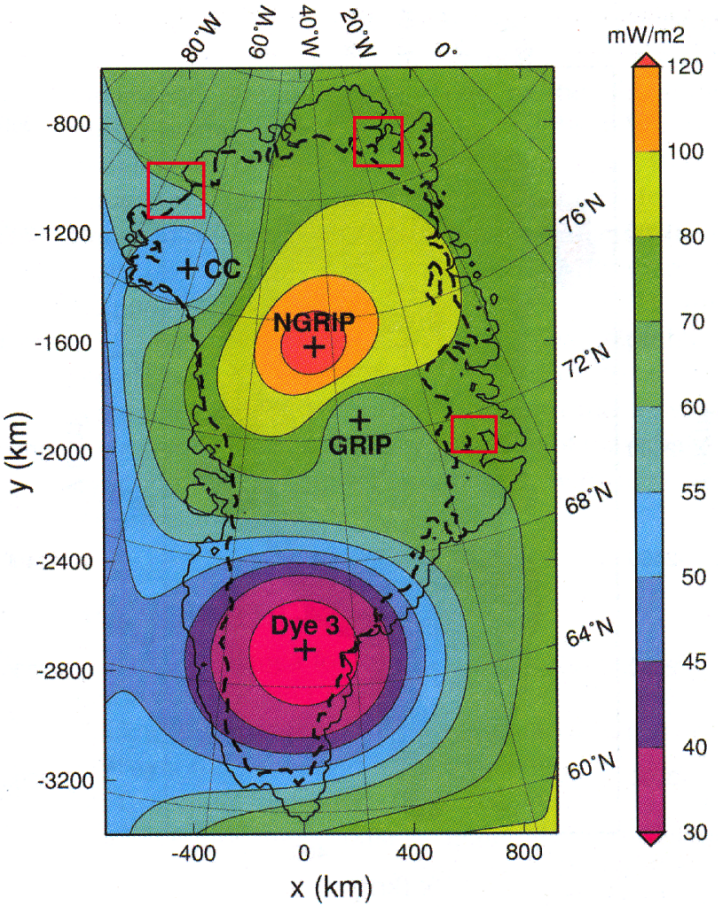

Figure 2.2: Map of modelled geothermal heat flux for Greenland constrained by direct measurements from ice core sites (labelled). Ice margin is delineated by dashed black line and glacier sites analysed in this study are marked by red boxes [Adapted from Greve, 2005].

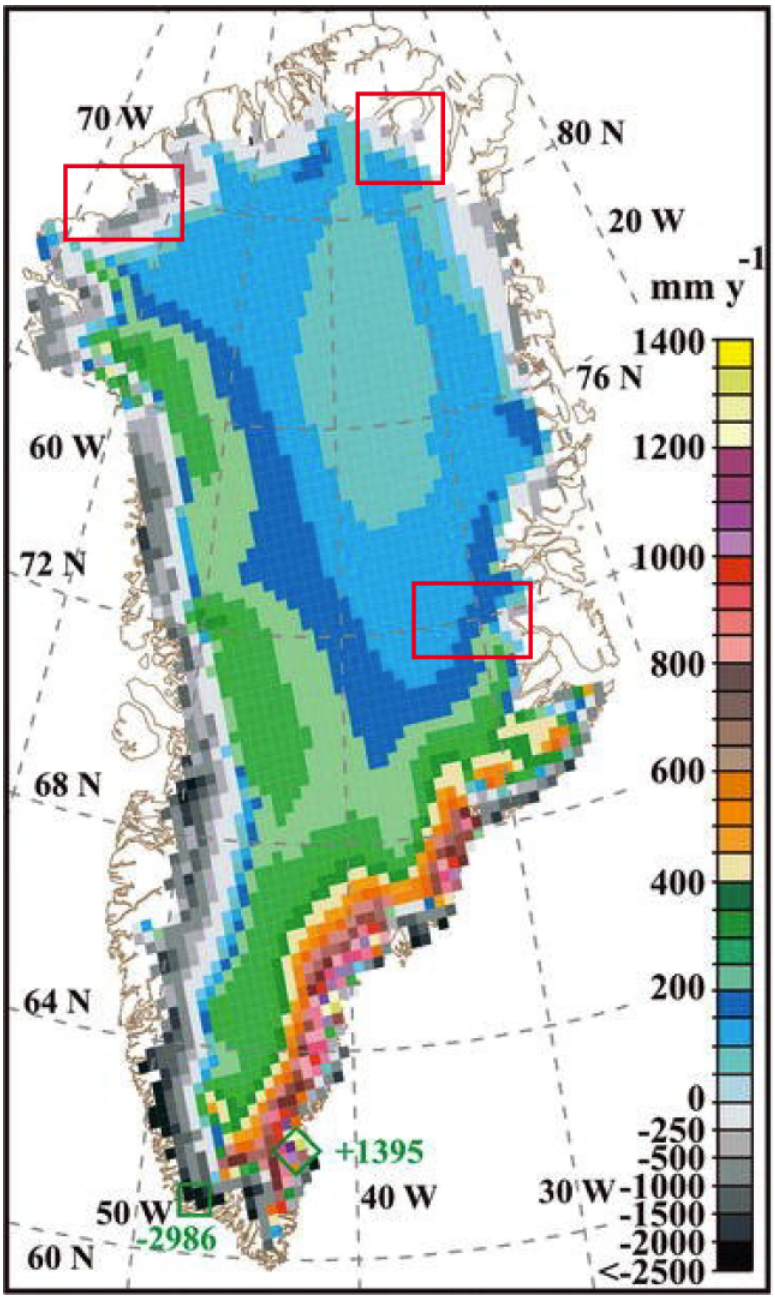

Figure 2.3: Map of modelled surface mass balance for Greenland using the regional climate model, Polar MM5. Values represent average annual surface mass balance from 1988-2004. Glacier sites analysed in this study are marked by red boxes [Adapted from Box et al., 2006].

Chapter 3

The Flow of Ice

Dedicated surveys of glaciers and ice sheets have highlighted the spatial variability in the speed of ice flow [e.g. Joughin et al., 2010; Moon et al., 2012]. The results from various experiments employing a range of methodologies, from simple laboratory tests through to elaborate computer models, have shown that bodies of ice exhibit complex internal stress interactions, which in turn drive two fundamental processes that facilitate ice motion: international deformation of the ice itself, known as creep, and slip at the interface between the ice and the bed. In general, ice flow by creep dominates in the slow flowing interior of ice sheets and some large glaciers, where temperatures are colder and ice is mostly frozen to the bed. Towards the margins and lower reaches however, slip at the bed becomes more dominant as pressure-induced melting of the ice lubricates the bed, allowing ice to move at faster speeds. The interplay between these two processes is of course not so simple, and variables such as temperature, the bed substrate, and the configuration of the subglacial hydrological system are highly influential. As such, the spatial variability of ice motion is a manifestation of these processes. The response to future change is therefore uncertain, and consequently accurately constraining conditions at the bed is an ongoing research field in glaciology.

In this chapter, the current state of knowledge on these processes is reviewed, and then applied to tidewater-type glaciers, as analysed in this study. A force balance approach is employed, which in its simplest sense assumes that there is no instantaneous acceleration of the ice and partitions stresses into driving and resistive components [van der Veen and Whillans, 1989], however where possible a means of calculating the velocity contribution of each mechanism is also provided. The approach adopted here therefore forms a robust framework with which one

can evaluate ice dynamic processes.

3.1 Ice Creep

The earliest investigations into the response of ice to an applied stress [e.g. Glen, 1952, 1953; Jacka, 1984] revealed that upon entering a state of plasticity, ice deforms in three phases (Fig. 3.1). In the primary creep phase, the strain rate decreases non-linearly to a minimum. The strain rate then non-linearly increases again in the secondary creep phase before reaching a steady state strain rate in the tertiary creep phase. This pattern of deformation occurs due to micro scale processes, such as slip along cleavage planes or dislocations within individual ice crystals, or softening due to recrystallisation between ice crystals [Glen, 1955]. However, additional variables such as the orientation of crystals, known as the ice fabric, and impurities within the ice may also affect this response [Jones and Glen, 1969; Cuffey et al., 2000].

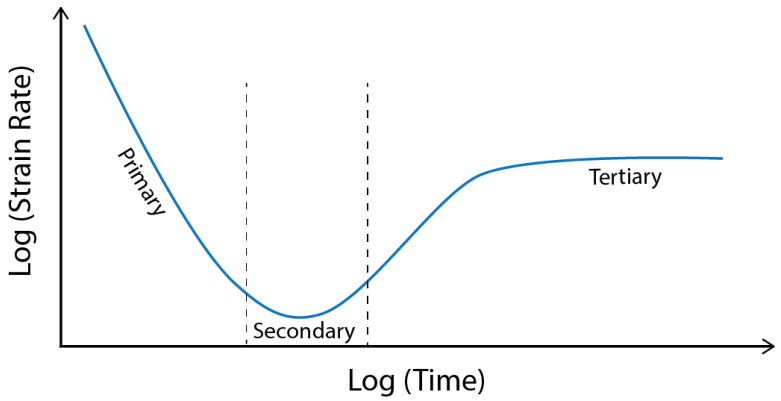

Figure 3.1: The typical response of polycrystalline ice to a constant applied stress, following initial elastic deformation (not shown). Creep phases are labelled. [Adapted from Cuffey and Paterson, 2010]

In ice sheets and glacier systems, the secondary and tertiary creep phases have both been shown to be important in regions of creep-dominated flow [Duval et al., 2000; Marshall, 2005]. However, the ease of identifying and characterising secondary creep, based on the minimum in the creep curve, means that traditional theory has commonly focused solely on this phase of deformation. In addition, Cuffey and Paterson [2010] argue that the response of ice under the typical magnitude of driving stresses found in these creep-dominated regions (50-150 kPa) is more consistent with secondary creep. Driving stress at the base of the ice may be

broadly calculated from the surface slope and the ice thickness, such that:

$$\tau_d = \rho_i \; g \; H \; tan\theta_s \tag{3.1}$$

Where τ_d is the driving stress (kPa), ρ_i the density of glacial ice (917 kg m^{-3}), g the acceleration due to gravity (9.81 m s^{-2}), H the ice thickness (m), and θ_s the surface slope of the ice. The secondary creep of ice was first described quantitatively by Glen's Flow Law [Glen, 1955], and later adapted for glaciers by Nye [1957]. It states that:

$$\dot{\varepsilon} = A \; \tau^n \tag{3.2}$$

Where $\dot{\epsilon}$ is the shear strain rate (s^{-1}), A a flow parameter dependent on temperature, and τ^n the shear stress to the power of n, a creep exponent usually taken as 3. The power law highlights the non-linearity of the deformation, and the inclusion of the flow parameter, A, is important because it emphasises the temperature dependence of the strain rate of ice. For warmer temperatures, ice deforms more readily as dislocations within ice crystals become more mobile, and crystal boundaries become more lubricated from melting [Goodman et al., 1981]. The exact value of A may be calculated from an Arrhenius-type relationship, adapted for glacial ice by Hooke [1981]:

$$A = A_0 \; exp\left(-\frac{Q^*}{R_g \; T_i} + \frac{0.498}{(T_0 - T_i)^k}\right) \tag{3.3}$$

Where A_0 is the prefactor coefficient (9.302 x 10^{-2} Pa^{-3} yr^{-1}), Q^* the activation energy for ice creep (7.88 x 10^4 J mol^{-1}), R_g the gas constant (8.314 J mol^{-1} K^{-1}), T_i the ice temperature (K), T_0 the melting point of ice (273.39 K), and k a constant (1.17).

As mentioned as the beginning of this chapter, creep is generally dominant in areas of slow flow in the interior of the ice sheet. To calculate the exact contribution of creep to ice velocities in these regions, one needs to consider the vertical strain rate profile through a column of ice. From Equation 3.2, the highest strain rates will occur where the highest shear stresses are located. Since ice is typically frozen to the bed in the interior, the highest shear stresses are therefore found at the bed. This means that strain rates are highest here, and decrease towards the surface. To calculate the surface velocity, one therefore needs to combine Equation 3.1 for stress with Equation 3.2 for strain rate, and then integrate over the entire ice thickness, H. This produces the following equation for surface velocity [Benn and

Evans, 2010]:

$$u_{sfc} = \frac{2A}{n+1}(\rho_i \; g \; tan\theta_s)^n \; H^{n+1} \tag{3.4}$$

Where u_{sfc} is the magnitude of the surface velocity (m yr^{-1}). In reality however, surface velocities in the interior of ice sheets will differ from those calculated by Equation 3.4. This is because whilst creep plays an important role in slow flowing ice, rarely is ice completely frozen to the bed, due to the effect of pressure-melting. The significance of this is discussed next.

3.2 Basal Slip

Due to the pressure dependence of the melting point of ice, which is depressed at a rate of 0.6°C km^{-1} depth [Bell, 2008], basal slip often plays a significant role in controlling ice flow, even in the interior of ice sheets. Indeed, Cuffey et al. [1999] found that high solute concentrations were also capable of maintaining thin (20-40 nm) water films at the base Meserve Glacier in Antarctica, where temperatures are as low as -17°C. The ability of ice to transition into a liquid state at the base of large ice sheets has therefore led to the development of a number of basal sliding theories. Until the 1980s, glaciers were assumed to slide over hard bedrock and early ideas focused on the effect of form drag created by bed obstacles (Section 3.2.1). Later, the influences of cavitation and subglacial hydrology were realised, and this continues to form an important component of glaciology, given recent and future projected increases in surface melting (Section 3.2.2). Observations at the beds of glaciers then turned attention to bed roughness and the associated frictional drag (Section 3.2.3), later leading to the so-called 'paradigm shift' in glaciology [Boulton, 1986], where observations revealed the existence of soft, deformable beds comprised of porous sediment (Section 3.2.4). The evolution of sliding theories with respect to these developments is now reviewed.

3.2.1 Hard Bed Sliding

The fundamental processes through which ice slides over a hard bed were first postulated in the seminal work of Weertman [1957]. He proposed two mechanisms to overcome form drag produced by obstacles at the base of glaciers: regelation and enhanced creep.

Where ice encounters an obstacle on the bed, a region of higher pressure is created

on its upstream side. This locally depresses the melting point of the ice and generates a film of meltwater, which follows the pressure gradient and therefore flows around the obstacle to its downstream side (Fig. 3.2). Here, the pressure is lower and so the melting point increases again and the water refreezes. The refreezing process releases latent heat, which is conducted through the obstacle to further aid melting at the upstream face. This process is known as regelation, and demonstrates that by turning to water, ice is able to flow around small obstacles it encounters at the bed. As the obstacle size increases however, the heat conduction becomes progressively more inefficient and so regelation is mostly restricted to obstacles smaller than 1 m in size.

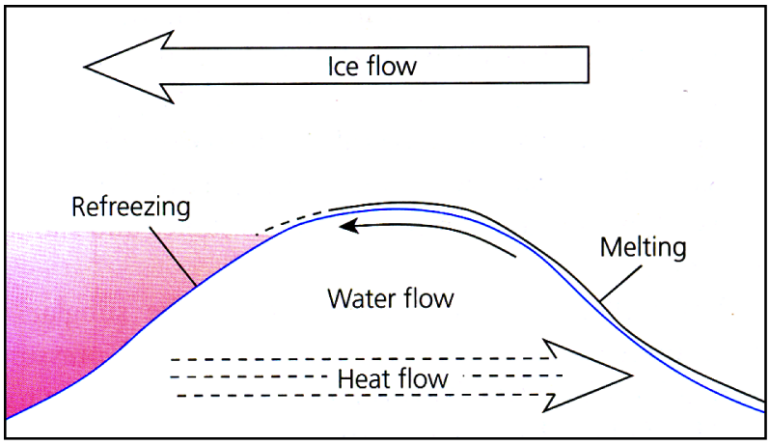

Figure 3.2: Schematic diagram illustrating how ice is able to flow over an obstacle through regelation. [Benn and Evans, 2010]

Although heat conduction is poor, stress concentrations around obstacles greater than 1 m continue to increase. As Glen's Flow Law states (Equation 3.2), the strain rate of the ice increases non-linearly with the applied stress, and so larger obstacles create locally high strain rates. In fact for n= 3, a doubling of the stress produces an 8-fold increase in the strain rate. Therefore ice can efficiently deform around larger obstacles, in a process known as enhanced creep [Weertman, 1967].

The sliding velocity from each mechanism can be combined to produce a version of Weertman's sliding law [Cuffey and Paterson, 2010]:

$$u_b = constant \cdot \left[\frac{\tau_b^{1/2}}{R}\right]^{n+1} \tag{3.5}$$

Where u_b is the basal sliding velocity (m yr^{-1}), R the bed roughness as a function of obstacles per unit area, and *constant* the product of a series of parameters

related to the material properties of the ice and bedrock. Importantly, Equation 3.5 also shows that for n= 3, the sliding velocity from regelation and enhanced creep varies with the square of the basal shear stress and inversely with the fourth power of the bed roughness. In other words, Weertman's approach requires very high stresses or otherwise produces very low sliding velocities. Furthermore, the sensitivity to the bed roughness means that only unrealistically smooth beds will be able to support reasonable sliding velocities [Fowler, 2011]. Although later refinements took into account more realistic conditions such as varying obstacle size [Weertman, 1964], different bed topographies [Kamb, 1970], and non-linear fluids [Fowler, 1981; Gudmundsson, 1997] these had little overall effect [Cuffey and Paterson, 2010]. Thus, a bigger picture was needed in order to explain the faster sliding velocities observed on real glaciers.

3.2.1.1 The Role of Hydrology

One of the assumptions in Weertman's theory was that apart from a thin film of water, ice is always in contact with the bed. This was captured by Lliboutry [1959], who proposed a third process, known as cavitation, that could operate in addition to regelation and enhanced creep. He argued that where ice encountered an obstacle at the bed, it could separate on the leeside to produce a cavity that could be maintained due to the presence of pressurised water at the base of the ice. The presence of water-filled cavities on the leeside of obstacles locally reduces the drag, enabling fast glacier flow. Furthermore, by reducing the drag on the leeside, the drag on the upstream side is increased, and so regelation and enhanced creep become more efficient. To assess the potential for cavitation to occur, some measure of the coupling of ice to the bed is required, and this is often expressed in terms of the effective pressure at the bed:

$$N_p = P_i - P_w \tag{3.6}$$

Where N_p is the effective pressure (Pa), P_i is the ice overburden pressure equal to $\rho_i g H$, and P_w the water pressure. The minimum effective pressure needed to decouple the ice from the bed is known as the separation pressure, P_s, and is therefore equal to P_w when separation occurs. If P_w continues to increase beyond P_s, separation increases and the cavities enlarge. Where cavities are larger and the value of N_p is low, less of the ice is in contact with the bed and so it can flow faster. By accounting for the effect of N_p, an improved version of the Weertman

relation (Equation 3.5) can be defined [Budd et al., 1979]:

$$u_b = k\ \tau_b^p\ N_p^{-q} \tag{3.7}$$

Where p and q are constants, equal to 3 and 3.5 respectively for tidewater glaciers [Nick, 2006]. Whilst Equation 3.7 successfully reproduces the behaviour of some glaciers, in particular their ability to stabilise at pinning points [Benn et al., 2007], it infers a close coupling between the bed and the ice and therefore (wrongly) suggests that basal drag will increase indefinitely with the sliding rate. This limitation partially arises by its neglecting of lateral drag, which becomes significant at tidewater margins where the fastest flow speeds are attained. Iken [1981] suggested that there must be an upper limit based on the bed geometry for Equation 3.7, such that:

$$\frac{\tau_b}{N_c} \leq tan\theta_c \tag{3.8}$$

Where θ_c is the angle between the obstacle and the bed slope angle. This consideration has been shown to hold true for both simple linear viscous fluids [Schoof, 2005] and more realistic non-linear fluids [Gagliardini et al., 2007]. Beyond this threshold, lateral drag becomes significant; this is discussed further in Section 3.3.

Effective pressure is therefore a key parameter to include in theories of sliding and recently there has been a focus on understanding how projected changes in climate will impact the role of effective pressure in controlling ice flow speeds. The seminal work of Zwally et al. [2002] showed that a major influence is likely to come from increased supraglacial melting in response to warmer temperatures, and the close coupling of the supraglacial and subglacial hydrological systems. Indeed they discovered a strong correlation between global positioning system (GPS) measurements of ice motion and surface melting from a Positive Degree Day (PDD) model at Swiss Camp in west-central Greenland. They speculated that the delivery of surface meltwater to the bed of the ice sheet was lubricating the ice-bed interface and permitting faster flow. Conversely when the summer melting ceased, ice decelerated. The implication of this was that future warming would lead to rapid flow speeds across the entire Greenland Ice Sheet. Their findings were supported by, among others, Bartholomew et al. [2010] who analysed a 35 km transect across the western flank of the Greenland Ice Sheet near Russell Glacier. In particular, they found that greater acceleration occurred further inland, but also that ice began to decelerate before the end of the summer melt season. The

authors attributed this to a reconfiguration of the subglacial hydrological system to a more efficient, channelised system once a threshold water pressure was reached. It is unclear whether this threshold changes inland, however the greater sensitivity to water inputs here may be simply attributed to the higher effective pressures here in general. Further validation of their findings was provided by Schoof [2010], who used a numerical model capable of switching between an inefficient, distributed drainage mode and an efficient, channelised drainage mode. He found that the greatest acceleration in flow was attained when the melt supply variability was greatest because this produced short-term increases in water pressures. Thus, the nature in which water is added to the subglacial hydrological system, rather than the sheer volume of water, will have the most important impact on ice motion. Contrary to Zwally et al. [2002], the relationship between effective pressure and future climatic change is not straightforward, and more observations are clearly required.

3.2.1.2 The Role of Debris

The discussion so far has assumed that it is clean ice sliding over bedrock. Of course in reality, the erosive action of glaciers entrains debris at the base and so driving stresses are actually resisted at the bed by both form drag from discrete obstacles, and frictional drag from a more continuous layer of debris-rich ice at the base. Although often overlooked, theories of sliding should technically represent stress as $\tau_b + \tau_f$, where τ_f is the stress from frictional drag due to debris. The magnitude of τ_f is especially dependent on the velocity component perpendicular to the local bed slope, and may be defined as [Cuffey and Paterson, 2010]:

$$\tau_f = k\ \mu\ C\ \eta_i\ \bar{u_n} \tag{3.9}$$

Where μ is the coefficient of friction for the bedrock, C the debris concentration (%), η_i the effective viscosity of the ice, and $\bar{w}$ the average component of the velocity perpendicular to the bed slope (m yr^{-1}). In general, there are few observations to constrain predictions of frictional drag and therefore it is considered by rarely implemented in studies involving where bed conditions are required. One notable study was however performed by Iverson et al. [2003] at the Svartisen Subglacial Laboratory in northern Norway. As part of a hydroelectric project, a series of tunnels allow access to the bed of Svartisen ice cap, and by placing a granite panel in contact with the ice, they were able to measure bed friction from

entrained debris. For debris concentrations ranging from 2 – 11%, a frictional stress of 60 – 200 kPa was produced, representing a more significant component to total resistive stress than that from form drag. A general lack of observations precludes its incorporation more widely in numerical models, however the role of debris should nevertheless remain an important consideration when analysing the basal boundary condition of glaciers and ice sheets.

3.2.2 Soft Bed Sliding

Debris at the base of glaciers is not purely restricted to entrainment in ice. Indeed, rather than hard bedrock, the beds of some glaciers have been shown to consist of soft sediment known as till. This sediment either originates from the in situ geology, which may consist of soft sedimentary strata, or as a product of glacial erosion. The classic evidence for soft bedded glaciers came from the Siple Coast ice streams in West Antarctica, where seismic reflection surveys revealed a highly porous till layer some 5-6 m thick at the base of the Whillans Ice Stream [Alley et al., 1986], although later work refined the actively deforming layer down to just the top 3 cm [Engelhardt et al., 1990; Engelhardt and Kamb, 1998]. These findings supported previous work at Breidamerkurjokull in Iceland, which showed that till saturated with water could deform at very lower shear stresses [Boulton and Jones, 1979], because high pore water pressures reduce grain-grain contact. Although initial models of its behaviour treated the till as a Bingham fluid, whereby the strain rate depended quasi-linearly on its strength [e.g. Boulton and Hindmarsh, 1987], laboratory tests of samples from Ice Stream B at the Siple Coast found that the strain rate of the till had little dependence on its strength [Kamb, 1991]. Further geotechnical tests by Tulaczyk et al. [2000] found that the failure strength of the till was instead strongly dependent on the effective stress of the till, rather than the strain rate, thereby supporting a Couldomb-Plastic rheology. They amended this to account for till compressibility, often represented in terms of till porosity, and proposed that subglacially deforming till follows a Compressible-Coulomb-Plastic model. The residual strength, τ_*, dependent on effective stress, is therefore defined as a Mohr-Colulomb rule, where:

$$\tau_* = c_0 + N_s \, tan\varphi \tag{3.10}$$

Where c_0 is the apparent cohesion, N_s the effective normal stress equal to $\sigma_n - P_w$, where σ_n is the compressive normal stress, and φ is the internal friction angle. The

effect of porosity is accounted for implicitly by c_0 and φ [Tulaczyk et al., 2000]. Deformation usually occurs in the upper layers of the sediment and is referred to as soft-bed sliding, although in some cases deformation takes place at depth as a sequence of shear planes are setup within the sediment layer due to the effects such as dilatancy (increases the yield stress of sediment due to limited volumetric expansion in response to an applied stress), and irregular clast size [Clarke, 2005]. In either case, effective pressure is highly influential and lower effective pressures lead to swelling of the sediment, which permits deformation more readily.

The velocity from soft-bed sliding or deformation may be calculated from [Cuffey and Paterson, 2010]:

$$u_b = u_{ss} + \int_Z \frac{du}{dz}\, dz \tag{3.11}$$

Where u_{ss} is the soft bed sliding velocity (m yr^{-1}), and z is the sediment thickness (m) such that the right hand term is the total contribution to velocity from deformation of the sediment with depth. In Greenland, there are few direct or indirect measurements of the bed conditions, and it is therefore generally assumed that glaciers slide over hard beds, although some recent evidence has controversially suggested soft bed sliding beneath parts of Jakobshavn Isbrae based on gravity and magnetic profiles [Block and Bell, 2011].

3.3 Fast Flowing Tidewater Glaciers

The final section of this chapter draws on the discussion so far surrounding mechanisms of ice flow and applies it to the glacier type analysed in this study: those which are fast flowing and terminate in tidewater. The marine environment at the terminus perhaps represents the most obvious characteristic of these glaciers, yet arguably also the most important. Fundamentally, sea level sets the base level for the subglacial hydrological system [Meier et al., 1994], meaning that basal water pressure is normally high, and therefore the effective pressure is low. As already discussed, this decouples the ice from the bed, reducing basal drag and leading to higher flow speeds. For polar tidewater glaciers in particular, the terminus may be even be fully floating [Meier and Post, 1987]. Since water pressure exerts a negligible drag on the base of ice, and observational evidence shows that tidewater glaciers do not accelerate indefinitely, then resistance to flow must be adopted by some other component of the force balance. This is revealed by further observa-

tional evidence which often displays arctuate crevasse distributions in the terminus region, and the constraint of glaciers to constrictions in the fjord geometry, thus pointing towards the lateral margins as the principle provider of resistive stress here [van der Veen, 2002]. The narrow fjords through which tidewater glaciers typically terminate create zones of high shear stress at the lateral margins. Sufficient resistance is provided to prevent infinite acceleration of the ice, however fast flow still occurs because shear-heating leads to fabric alignment within the ice, and a reduction in its yield stress. Equation 3.4 in Section 3.1 provided a method to calculate surface velocity from ice creep. Where velocity is uniform with depth (i.e. little resistance at the bed), but non-uniform across the glacier (from lateral shear) as is the case at tidewater margins, then the centreline velocity component may instead be defined as [Benn et al., 2007]:

$$u_{ctr} = \frac{2A}{n+1}\left(\frac{\tau_d}{H}\right)^n W^{n+1} \tag{3.12}$$

Where u_{ctr} is the centreline velocity (m yr^{-1}) and W the half-width of the glacier (m). Thus lateral stress provides an important buttressing effect for tidewater glaciers.

In accelerating to the fastest flow speeds however, a longitudinal stress gradient is also established along the course of the glacier. Transverse crevasses often represent the surface expression of this stress component as ice thins and extends, and recent thinning on tidewater glaciers has been accompanied by acceleration and retreat [e.g. Howat et al., 2008], highlighting the role of longitudinal stress in controlling terminus stability. The loss of ice in the terminus region reduces the magnitude of lateral stress that can be applied, leading to substantial increases in velocity, best demonstrated by Jakobshavn Isbrae in west Greenland [e.g. Joughin et al., 2004]. Early work suggested that fjord depth was closely related to calving frequency, due to the effect of buoyancy [Pelto and Warren, 1991]. This has been supported by evidence of the synchronisation of calving with tidal cycles, which can create additional flexure at the terminus [Meier and Post, 1987; O'Neel et al., 2003]. Indeed, these ideas may explain recent retreat in Greenland where tidewater glaciers terminate in deeply incised fjords [Morlighem et al., 2014]. More recently, disintegration of large ice shelves has been attributed to the presence of water in surface crevasses, which adds hydrostatic pressure to existing tensile stresses, promoting crevasse propagation [Scambos et al., 2000, 2009]. This hydrofracturing

process also provides a positive feedback mechanism, whereby increased melting in line with predictions of higher air temperatures drives more frequent calving at tidewater termini. Most recently, the intrusion of warm subtropical waters into fjord systems is thought to contribute to calving rates by undercutting the termini of tidewater glaciers through strong forced convection due to the interaction with cold, fresh meltwater discharged subglacially by tidewater glaciers [e.g. Rignot et al., 2010; O'Leary and Christoffersen, 2013].

Thus the fast flow speeds observed on tidewater glaciers are a manifestation of reduced drag at the base of the ice due to lower effective pressures as ice approaches flotation, and influence of calving on reducing the backstress generated by drag at their lateral margins.

Chapter 4

Data and Methods

This research utilises data collected from airborne geophysical surveys in 2011 and 2012, as well as a variety of freely available data, a novel methodology for creating high-resolution bed topographies, and a high-order 3D glaciological model. Their application are presented here in turn.

4.1 Datasets

4.1.1 Ice Thickness

In recent years, a number of airborne geophysical campaigns have been run in Greenland in order to more accurately resolve the bed topographies of glaciated terrain. Among a suite of instruments, these campaigns typically employ radar sounders, which produce echograms of the surface, internal layers, and perhaps most importantly, the bed. Processing algorithms then extract quantitative data from these echograms in the form of discrete ice thickness points along each flight line, with a vertical error of up to 50 m [Morlighem et al., 2013]. The data is tagged with GPS and time information allowing spatial analysis to be performed.

This research utilises ice thickness data from two large field programs in Greenland. The main source of data was the Greenland Outlet Glacier Geophysics (GrOGG) project run jointly by the University of Cambridge and the University of Texas. This program flew the High Capability RadarSounder-2 (HiCARS-2), developed by the University of Texas Institute for Geophysics, on board a BT-67 aircraft during the summer field seasons of 2011 and 2012. The radar operates at 60 MHz with a 15 MHz bandwidth and echograms were processed using synthetic aperture

radar (SAR) focusing, developed from previous missions, to improve along-track resolution [Peters et al., 2005, 2007; Palmer et al., 2013; Young et al., 2011]. Full-focusing was not complete at the time of writing, however ice thickness data was still available from this survey to an approximate uncertainty of 50 m.

This dataset was supplemented by the Operation IceBridge (OIB) mission run by the National Aeronautics and Space Administration (NASA). Whilst initially designed simply to maintain measurements of ice sheet change before the arrival of the Ice, Cloud, and land Elevation Satellite-II (ICESat-II) in 2016, the campaign has since produced a comprehensive dataset of ice thickness measurements over the majority of Greenland [Li et al., 2013]. Since the start of the program in 1993, a series of radar sounders have been flown using P-3B and DC-8 aircraft. The Multi-channel Coherent Radar Depth Sounder (MCoRDS), developed by the University of Kansas and the Centre for Remote Sensing of Ice Sheets (CReSIS), has been used since 2010 [Gogineni et al., 2001]. The instrument operates at frequencies of 180-210 MHz with a 10-30 MHz adjustable bandwidth, and is equipped with multiple receivers to reduce cross-track noise, thereby allowing weak bed echoes to be detected [Bamber et al., 2013]. The years from which survey data were used in this study are summarised in Table 4.1 below.

Table 4.1: Ice thickness data used for each study site by campaign and acquisition year(s)

Campaign	Daugaard-Jensen Gletscher	Academy Gletscher & Hagen Brae	Humboldt Gletscher
GrOGG	2011	2012	2012
OIB	2011, 2012	2012, 2013	2010, 2011, 2012, 2013

4.1.2 Surface Elevation and Ice Mask

Surface elevation data was derived from a Digital Elevation Model (DEM) of the ice surface, which is part of the Greenland Ice Mapping Project (GIMP) dataset [Howat et al., 2014]. The surface DEM merges and improves pre-existing DEMs [Scambos and Haran, 2002; Bamber et al., 2001b] by including photogrammetric topography data and laser altimetry data from ICESat-I. It offers a spatial resolution of 15 m, and can therefore be used more effectively with other remote sensing products which typically operate at a similar resolution.

The dataset also includes a land classification mask of the same resolution for delineating areas of ice-free terrain. The mask is produced from a complete im-

age mosaic of the ice sheet, using Landsat-7 ETM+ and RADARSAT-1 imagery acquired from 1999-2002.

4.1.3 Surface Velocity

Surface velocity data was sourced from the NASA's Making Earth System Data Records for Use in Research Environments (MEaSUREs) program [Joughin et al., 2010]. The dataset produces annual velocity maps of Greenland gridded to 500 m resolution, and for selected fast-flowing outlet glaciers, more detailed maps at 100 m resolution. The velocity maps are created using speckle tracking and interferometric algorithms [Joughin, 2002] with RADARSAT-1 InSAR data for 500 m products and TerraSAR-X image pairs for selected glaciers at 100 m resolution. Table 4.2 summarises the image pairs and velocity maps selected for use in this study.

Table 4.2: Surface velocity data used for each study site by satellite and acquisition date (DD-MM-YY)

Satellite	Daugaard-Jensen Gletscher	Academy Gletscher & Hagen Brae	Humboldt Gletscher
RADARSAT (500 m)	2008/9	2008/9	2008/9
TerraSAR-X (100 m)	12-3-11 / 23-3-11 27-3-11 / 07-4-11 28-3-11 / 08-4-11	27-3-11 / 07-04-11 08-3-11 / 19-03-11	15-3-11 / 26-3-11

4.1.4 Surface Mass Balance

Spatially continuous surface mass balance data was generated by the Regional Atmospheric Climate Model (RACMO2), developed by the Royal Netherlands Meteorological Institute (KNMI). The model has a spatial resolution of 11 km and outputs surface mass balance and surface runoff data at a monthly timescale from 1957 to present [van Meijgaard et al., 2008]. The annual average from 1957 to 2011 or 2012, depending on the airborne survey year, was used here. For a more detailed description of this model, the reader is referred to Ettema et al. [2009, 2010].

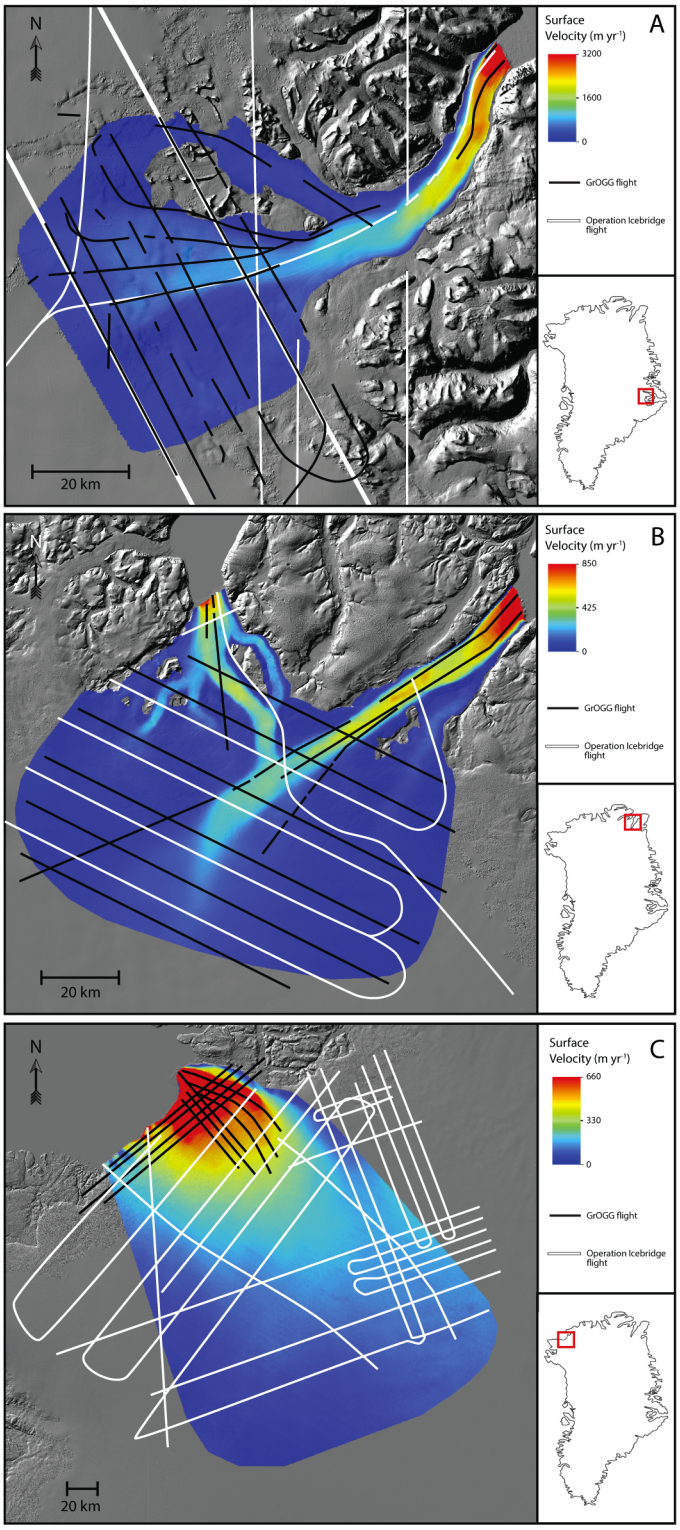

Figure 4.1: Summary of the data available at Daugaard-Jensen Gletscher (A), Academy Gletscher and Hagen Brae (B) and Humboldt Gletscher (C). White lines indicate OIB flights and black lines indicate GrOGG flights. Velocity data is from the MEaSUREs dataset, and the extent of the velocity map also delineates the model domain for each glacier. Background image is a hillshade map from the GIMP surface DEM.

4.2 Deriving Basal Geometry

Deriving accurate basal geometry is often a necessary precursor to investigations involving numerical modelling, and the majority of studies to date have achieved this through geostatistical techniques such as ordinary kriging. This approach offers a measure of accuracy known as the kriging variance and is a technique commonly used in the generation of bed topography for ice sheets [e.g. Bamber et al., 2001a, 2013]. However, it fails to emplace physical constraints related to the flow of ice, and therefore whilst effective in the interior of the ice sheet where flow velocities are low, the results in areas of fast flow near the margins of the ice sheet often deviate significantly from the true values, producing large ice flux divergence errors if subsequently employed in ice flow models [Seroussi et al., 2011]. Further inaccuracies are introduced due to the extrapolation of errors in the ice thickness data related to the presence of crevasses and steep topography which increase radar clutter, and supra- or en-glacial water storage which suppress bed echoes. The nature of ice thickness data itself, which consists of closely-spaced data points along flight lines spaced several kilometres apart, tends to produce erroneous artefacts such as 'bulls-eyes' around isolated depressions or high-stands, and problems may be further exaggerated by clustered data in densely surveyed areas (e.g. a glacier terminus) [Fretwell et al., 2013].

To resolve these issues, a two-stage approach to reconstructing complete bed topography was employed here. Near the margins of the ice sheet where geostatistical methods are less accurate, a relatively novel methodology was used, which relies on the principle of mass continuity to derive a continuous, high-resolution (100 m) ice thickness map. Inland, where mass conservation is less suitable, an algorithm known as Topogrid was used to interpolate ice thickness data. This has recently been successfully applied in the production of Bedmap2 for Antarctica by Fretwell et al. [2013] and rectifies some of the issues encountered when interpolating flight-line data with ordinary kriging. The two products were then integrated to produce a seamless map of ice thickness for each study site, which was then subtracted from the GIMP surface DEM to obtain bed elevations.

4.2.1 Mass conservation

The principle of mass conservation has existed in glaciology for several decades, since Rasmussen [1985] first developed an algorithm to minimise ice flux diver-

gence in surface ice velocity data at Columbia Glacier in Alaska. Although later calculating actual bed topography using a similar method [Rasmussen, 1988], the results of his and similar studies [e.g. Fastook et al., 1995; O'Neel et al., 2005] deviated significantly from the absolute values collected by radar sounding. Only recently has mass conservation been more widely employed as the availability of ice thickness measurements has increased and more sophisticated methodology developed to reduce errors, most notably that of Morlighem et al. [2011, 2013, 2014] for Greenland. McNabb et al. [2012] simplified their approach using flowlines rather than their computationally expensive finite element method, and it is this method that is used here.

In applying the mass conservation method, there are several requirements and assumptions that must be acknowledged. Perhaps most obviously, ice flow must be well-constrained by surface topography so that the mass is effectively conserved across the area to which the method is applied. For this reason, mass conservation was only applied to Daugaard-Jensen Gletscher, and Academy Gletscher and Hagen Brae, which are steered through well-defined fjords systems. The method corrects for any mass lost through surface ablation, however. Previous research has also shown that inferred thicknesses are sensitive to errors in the surface velocity data [Morlighem et al., 2014]. In this regard, the mass conservation method is therefore most accurate in areas of fast-flow (i.e. channelised outlet glaciers) where the uncertainty in the surface velocity data, typically 10 m yr^{-1} [Joughin et al., 2010], forms a smaller percentage of the total velocity at a specific location. One also assumes that the ice is flowing in a steady velocity field and so not accelerating or decelerating. Finally, ice thickness at a specific location is assumed to be represented as a vertical column of ice with uniform density. The method therefore neglects compaction of ice, and internal deformation so that the surface velocity is equal to the depth-averaged velocity. This is generally an accurate assumption on fast flowing outlet glaciers where most of the motion occurs through slip at the bed and the ice is ablating.

Having considered the assumptions above, a flux gate was first selected for each outlet glacier. Flux gates were preferably orientated perpendicular to the flow direction, resolved ice thickness well (i.e. were located along a flightline), and stretched across the entire width of ice. From here, flowline paths were plotted based on the trajectory of an imaginary particle through the surface velocity field

in an arbitrary time period. This was achieved using the Runge-Kutta-Fehlenberg 45 method (RKF 45), which automatically adapts the timestep size when plotting the particle trajectory, so that the trajectory error is minimised. Flowlines were spaced equally apart, at a distance that ensured they remained approximately parallel for the remaining course of the glacier, so that the initial flux from the flux gate remained a good approximation of the flux carried by each flowline [McNabb et al., 2012].

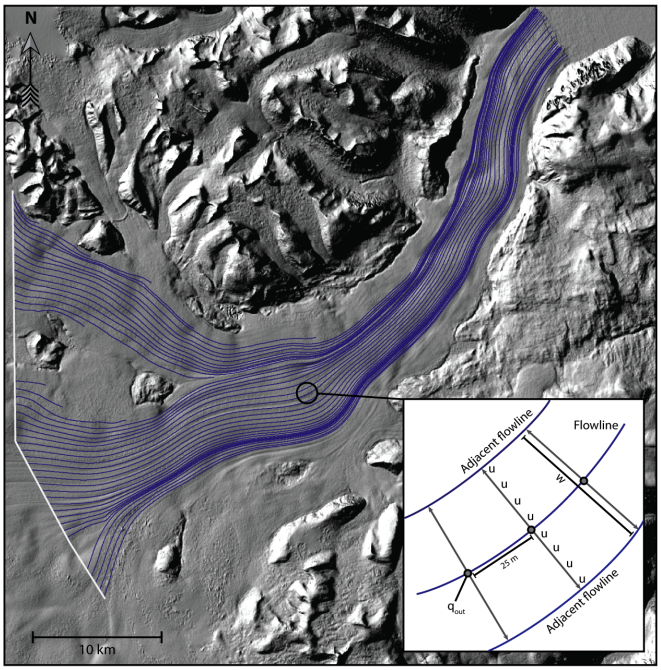

Figure 4.2: Example of flowline configuration for Daugaard-Jensen Gletscher, as used in applying the mass conservation method. Inset summarises how ice thickness is calculated for each point along the flowlines, where q_out is the flux conserved along each flowline, u is the velocity along each transect, and w is the flowline width.

Each flowline was then divided into equidistant points spaced 25 m apart, and a transect then created at each point. The length of the transect was determined by the distance to each adjacent flowline, with its orientation being perpendicular to the local orientation of the flowline point (Fig. 4.2). The surface velocity was then sampled along each transect and averaged.

From Cuffey and Paterson [2010], the long term evolution of an ice mass is defined as:

$$\frac{dH}{dt} = \dot{b} - \nabla \cdot \vec{q} \tag{4.1}$$

Where dH/dt is the change in ice thickness with time, here taken to be zero because ice is assumed to be in steady state, $\dot{b}$ the sum of the surface and basal mass balance rates (m yr^{-1}), and $\nabla \cdot \vec{q}$ the ice flux divergence. The basal mass balance rate is assumed to be negligible and therefore only the surface mass balance rate is corrected for so that $\dot{b}$ becomes b_{sfc}. As previously mentioned, ice is also assumed to be of uniform density and so ice thickness, H, becomes the ice-equivalent thickness, $\hat{H}$. In this scenario, $\vec{q} = \bar{u}H$, and so from McNabb et al. [2012], Equation 4.1 may be rearranged to solve for ice thickness at each flowline point, given an initial ice flux:

$$\hat{H} = \frac{q_{out} + \int b_{sfc}\, dS}{W_f\ \bar{u}} \tag{4.2}$$

Where q_{out} is the initial ice flux from the flux gate that is conserved along each flowline (m^3 yr^{-1}), b_{sfc} the surface mass balance for that point integrated over the length of the flowline to that point, W_f the width of the transect at that point (m), and $\bar{u}$ the mean velocity along the transect (m yr^{-1}).

The ice thickness dataset was then gridded to 100 m resolution using a moving-average algorithm. This method incorporates a user-defined search ellipse which helps smooth the ice thickness data, preventing erroneous steps between consecutive flowlines. Synthetic data was also generated for areas of ice-free terrain according to the GIMP land classification mask, to improve the gridding process and prevent unrealistic vertical cliffs close to ice margins.

4.2.2 Topogrid

In slower flowing regions such as further inland, the assumptions made for mass conservation become less valid. In particular, errors in the surface velocity field are greater, and ice is poorly confined by surface topography. Instead, interpolation using the Topogrid function in ArcGIS was used. Topogrid is based on the ANUDEM program, and produces hydrologically correct DEMs by coupling a thin plate spline function with an iterative finite difference interpolator that removes erroneous sinks or pits in the basal topography [Hutchinson, 1989]. By imposing drainage conditions, higher accuracy DEMs are produced with less data, and a roughness penalty allows the DEM to be fitted to abrupt changes in the input data, which in turn allows more dramatic topographies to be produced [Hutchinson, 1988]. A minimum z-value of 0 was imposed to prevent negative ice thicknesses

being produced, and the best results were found with drainage enforcement set to 'enforce with sink', the primary data type as 'spot', vertical standard error as 50 m, and maximum iterations and roughness penalty as the default values. Synthetic data was again created over known areas of ice-free terrain, determined using the GIMP ice mask, to help constrain the gridding process. The function was applied using a spatial resolution of 300 m, which represented the average flightline spacing. Topogrid was used to generate the entire bed DEM for Humdoldt Gletscher, and supplemented mass conservation for Daugaard-Jensen Gletscher and Academy Gletscher and Hagen Brae.

4.2.3 Bed Map Integration

In order to produce a continuous and seamless map of the bed topography for each catchment, the ice thickness maps from mass conservation and topogrid were integrated using a distance weighting process. The maps were clipped so that they overlapped by 10 pixels (10 km at 100 m resolution). Concentric buffers were then constructed each with an appropriate weighting. Each map was then multiplied by the weighting to adjust the pixel values in the overlap zone. The two maps were then added together to produce the final map of ice thickness from which bed elevations could be derived.

4.3 Numerical Modelling

The second aim of this study, to calculate basal drag, was addressed using a glaciological model. Numerical models are important tools in glaciology, providing process understanding and generating quantitative information that can be used for further statistical analysis. Previous research has often used more simple models that approximate or parameterise ice flow characteristics in, for example, the Shallow Ice or Shallow Shelf Approximation (SIA/SSA) method [e.g. Vieli and Payne, 2003; Rutt et al., 2009]. In recent years however, advances in computing permit the use of more computationally expensive models to solve complex problems using high-order physics and in 3D. Having derived high-resolution bed topographies for the selected glaciers, the Elmer/Ice model was therefore applied to solve for bed friction using surface velocity data with an inverse method.

4.3.1 Elmer/Ice

Elmer/Ice is an open source package that provides a framework for the physical modelling of glaciological problems. It is an extension of the Elmer package developed by the CSC-IT Centre for Science in Finland and solves Partial Differential Equations (PDEs), including the full Navier-Stokes equations, by using the Finite Element Method (FEM). The use of 'full-stokes' models has been shown to be essential when modelling the dramatic relief of outlet glaciers so as to account for important influences such as the bridging effect, where local changes in vertical normal stress affects the stress at the bed [Morlighem et al., 2010]. Furthermore, the FEM allows adaptation of the mesh resolution both spatially and temporally, which is not possible with the more commonly used Finite Difference Method (FDM). Perhaps most importantly for this study however, is the implementation of parallel computation which is essential for large datasets and inverse problems.

4.3.2 Mesh Generation

The meshes for the model were first constructed in 2D from a footprint of each glacier. This was determined by the position of the ice margin for each glacier catchment, either as an ice-rock boundary near the terminus, or as an ice-ice boundary further inland. The GIMP land classification mask was used to determine the former, and velocity vectors were plotted to determine the location of the latter. The 2D mesh was then created using the Gmsh software and a Delaunay triangulation algorithm. Previous studies have often scaled the mesh resolution with surface velocity data using mesh adaption software (e.g. YAMS [Frey and Alauzet, 2005]) to refine results in areas of fast flow [e.g. Seddik et al., 2012]. Whilst this improves computational efficiency, the results inland are of coarser resolution. The study sites in this investigation were sufficiently small to keep a constant but fine mesh resolution, which ensured that the bed characteristics further inland could also be captured in detail. The 2D mesh was then partitioned into 8 elements using the Serial Graph Partitioning and Fill-reducing Matrix (METIS) program, to facilitate parallel computation. Finally, upon initialisation of the model, the 2D mesh was vertically extruded into 3D across 10 equally-spaced layers to the topography of the surface and bed DEMs.

4.3.3 Forward Component

The forward component of the model was driven by the full Navier-Stokes equations. Ice was considered an incompressible and isotropic material within the model and its behaviour was influenced by its viscosity, here defined by Glen's Flow Law (Equation 3.2). A creep exponent of 3 was used and the rate factor A calculated using Equation 3.3 for a constant ice temperature of -10°C. The creep exponent has been shown to range from 1.5 – 4.2 in a range of environments [Weertman, 1983]. By taking the mean of this range, 3, a compromise can be made to account for the different magnitudes of stress that occur between the interior and terminus regions within each model domain. The same logic is applied when using a constant ice temperature of -10°C: measured borehole temperatures in the interior of the Greenland Ice Sheet have been found to typically range from 0 to -30°C [e.g. Johnsen et al., 1995]. Taking -10°C accounts for both the mean of this range and the extra addition of heat to the system through strain heating in high shear regions near the terminus, and the conduction of geothermal heat up through the ice. Correctly accounting for temperature in inversions is inherently difficult, primarily due to the lack of measurements. Whilst inversions for viscosity are indeed possible, previous research has found that spatially varying rheologies reduce the sensitivity of the basal friction coefficient to surface velocity data [Petra et al., 2012], reducing the accuracy of the friction inversion, and it was beyond the scope of this study to explore this further.

4.3.3.1 Boundary Conditions

Ice dynamics in the model were constrained by a number of boundary conditions. The upper surface was treated as a stress free surface. Accumulation, ablation and therefore free-surface evolution were ignored as the model was a static simulation. At the bed, a linear friction law was applied, such that:

$$\tau_b = \beta^2 \, u_b \tag{4.3}$$

Where β is the slip coefficient. Some previous studies have developed and utilised more complex non-linear friction laws [e.g. Gagliardini et al., 2007], however Morlighem et al. [2010] note that the choice of friction law is not essential in steady-state simulations and that the model generally converges on similar values of τ_b. At the inflow boundary, the observed surface velocity was imposed, whilst at lateral boundaries, a no slip condition applied, consistent with observations [e.g. Stearns, 2011]. A

sea pressure relation was imposed on marine boundaries, which related the depth below sea level to hydrostatic pressure in the following equation:

$$P_w = \rho_w \; g(z_x - h_w) \tag{4.4}$$

Where P_w is the hydrostatic pressure exerted normal to the marine boundary, ρ_w the sea water density (1027 kg m^{-3}), h_w the sea surface elevation, and z_x the elevation of a given node below sea level.

4.3.4 Inverse Component

Whilst Elmer/Ice supports both the Robin and Control (adjoint) methods for inversions, recent developments of the software now state that the control method should be the preferred method for inversions. Unlike the Robin method, non-linear viscosites can also be included (i.e. n > 1). After being initially adapted for glaciological applications by MacAyeal [1993], it has been successfully applied to full-stokes modelling in several recent studies [e.g. Morlighem et al., 2010; Gillet-Chaulet et al., 2012]. The method minimises a cost function, which represents the mismatch between observed and modelled velocities. The process is summarised below, although the reader is referred to Gillet-Chaulet et al. [2012]; Gagliardini et al. [2013] for more detailed descriptions. From Gillet-Chaulet et al. [2012], the initial cost function, J_0, is defined as:

$$J_0 = \int_{\Gamma_s} \frac{1}{2}(|u_H| - |u_H^{obs}|)^2 \; d\Gamma \tag{4.5}$$

Where u_H is the horizontal component of the modelled velocity (m yr^{-1}), and u_H^{obs} is the observed velocity (m yr^{-1}).

4.3.4.1 Regularisation

In order to avoid negative values of β being produced from the model, a power formulation is used to represent β, such that:

$$\beta = 10^{\alpha} \tag{4.6}$$

The minimisation of the cost function is now done with respect to α rather than β. Furthermore, a Tikhonov regularisation term, J_{reg}, is added to the cost function. This penalises spatial variations in the value of β, now termed α, to aid convergence

and optimisation of the model. J_{reg}, is defined as:

$$J_{reg} = \int_{\Gamma_b} \frac{1}{2}(\frac{d\alpha}{dx})^2 + (\frac{d\alpha}{dy})^2 \; d\Gamma \tag{4.7}$$

And the total cost function, J_{tot}, now reads:

$$J_{tot} = J_0 + \lambda J_{reg} \tag{4.8}$$

Where λ is a parameter that can be manually adjusted to alter the amount of penalisation by J_{reg}. The minimum of the cost function is now a balance of the optimum smoothness in α and the mismatch between modelled and observed velocities. This was varied to find the optimum value.

4.3.4.2 Minimisation

Minimisation of the cost function, J_{tot}, was done using the M1QN3 routine [Gilbert and Lemaréchal, 1989]. This implements a limited memory quasi-Newtonian iterative scheme and uses a line-search method with the second derivatives of the cost function to minimise J_{tot}. This is based on the Fletcher-Lemarchal algorithm, and is more efficient than a fixed-step minimisation. Convergence was aided by the Generalised Minimal Residual Method (GMRES) preconditioner and the iteration process was initialised with an initial guess for β, calculated from SIA theory.

4.4 Model Optimisation

Uncertainties in the model related to errors in input data (e.g. surface velocity measurements) meant that the value of the regularisation parameter, λ, was site-specific. To determine the optimal value for each study site, the L-curve method was employed [Hansen, 2001]. This method plots the regularised cost function, J_{reg}, against the initial cost function, J_0, to produce a characteristic L-curve where the corner objectively defines the best value of λ.

For Daugaard-Jensen Gletscher (Fig. 4.3A), J_0 actually increases when λ is increased from 0 to 10^7, despite a decrease in J_{reg}. J_{reg} then continues to decrease and J_0 now also decreases such that λ reaches the optimum value at 10^8. Thereafter, J_{reg} continues to decrease but only with a simultaneous increase in J_0. For Academy Gletscher and Hagen Brae (Fig. 4.3B), a similar pattern is observed:

from $\lambda = 0$ to $\lambda = 10^9$, J_{reg} decreases by nearly 1.5 orders of magnitude, with a concomitant decrease in the J_0. The best fit is found where $\lambda = 10^9$, after which J_{reg} continues to increase but only whilst J_0 increases. With Humboldt Gletscher (Fig. 4.3C), J_{reg} initially increases from $\lambda = 0$ to $\lambda = 10^7$ whilst J_0 decreases. J_{reg} then decreases by almost an order of magnitude, accompanied by a further decrease in J_0, to the optimal fit at $\lambda = 10^9$. Thereafter, J_{reg} continues to decrease but only with a coincident increase in J_0.

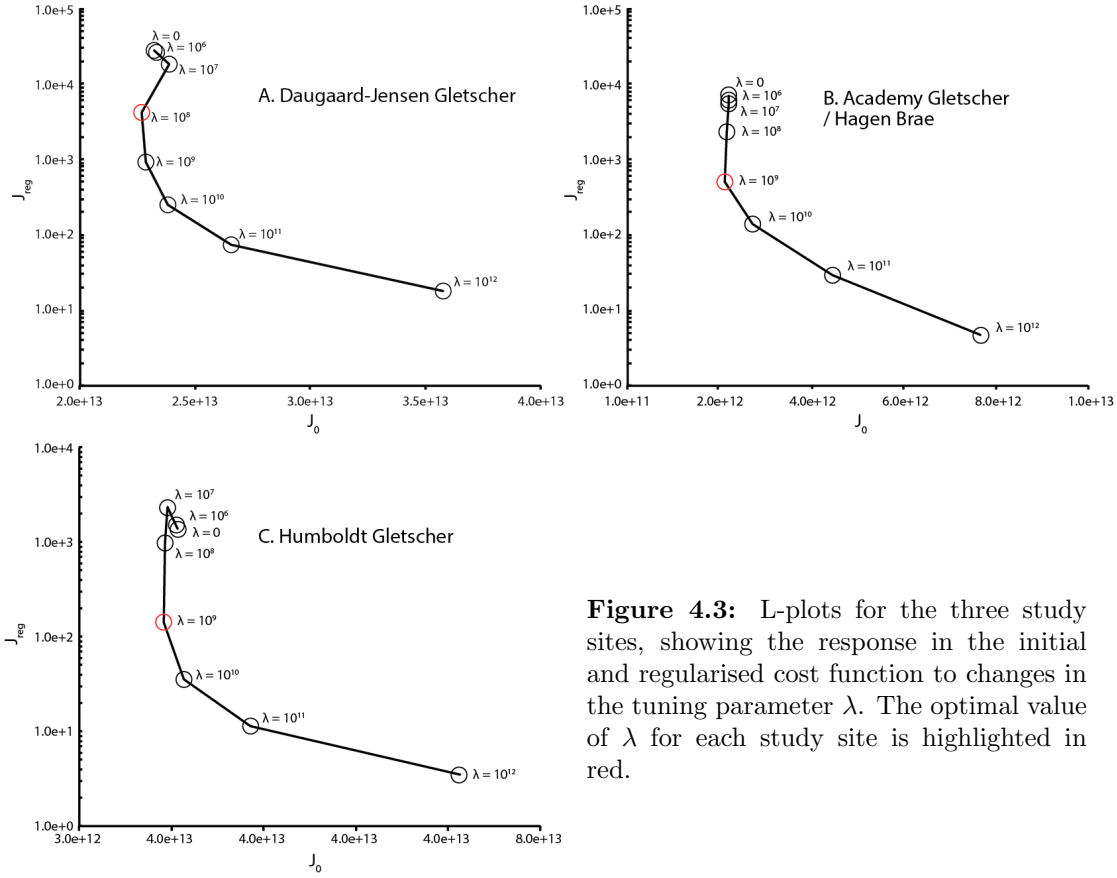

Figure 4.3: L-plots for the three study sites, showing the response in the initial and regularised cost function to changes in the tuning parameter λ. The optimal value of λ for each study site is highlighted in red.

Chapter 5

Results

This chapter presents the bed topographies and inversion results for each study site. Key findings are then summarised in the final section.

5.1 Daugaard-Jensen Gletscher

5.1.1 Flow and Setting

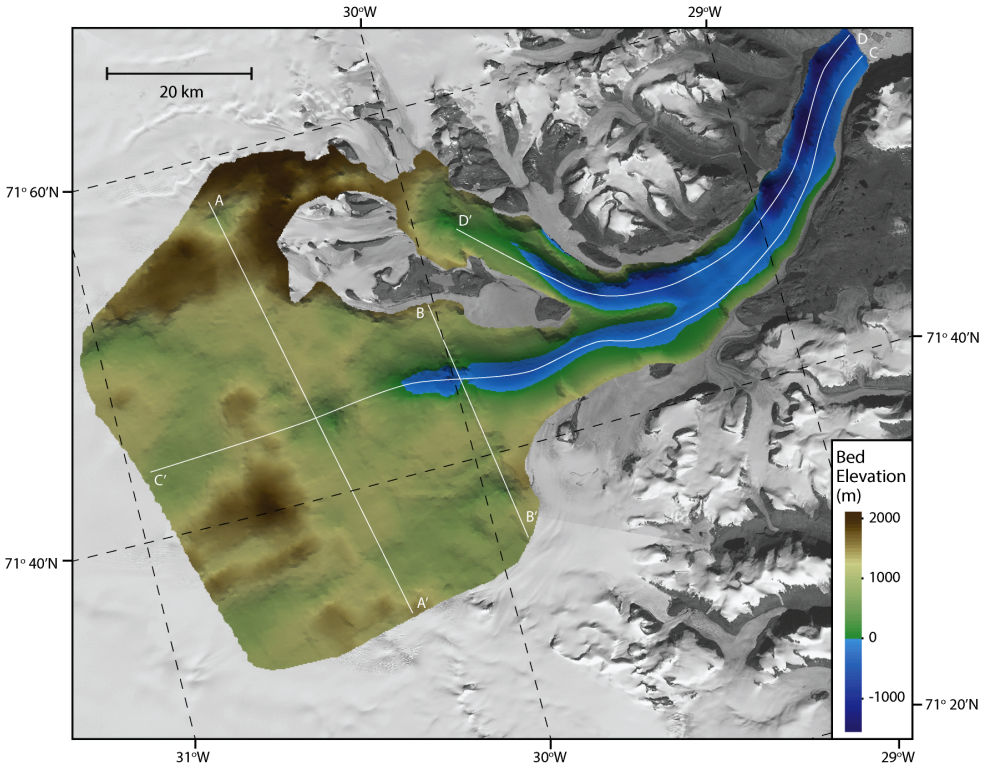

Figure 5.1: Map of bed topography for Daugaard-Jensen Gletscher, derived from mass conservation and inland interpolation, overlaid on a RADARSAT-1 image mosaic. White lines illustrate locations of transects analysed in Figure 5.3.

The bed topography of the Daugaard-Jensen Gletscher catchment (Fig. 5.1) exhibits dramatic relief, with a range in bed elevation of approximately 3000 m. Inland, ice flows across a high plateau surface with an average elevation of 1000 m above sea level. The undulating terrain, which ranges from 250 – 2000 m above sea level is consistent with slower ice flow in this region, particularly in areas of locally high bed elevation. At about 65 km from the terminus, ice is channeled into two small troughs, coincident with an increase in flow speed. The more southerly trough is both deeper and wider, accompanying slightly faster flow here. The troughs converge at 45 km from the terminus, although ice is partially divided by a 250 m high, longitudinally aligned bedrock ridge for a further 10 km. The main fjord lies almost entirely below sea level, and deepens towards the terminus, concomitant with ice acceleration to the fastest flow speeds. The cross-profiles of the troughs are generally U-shaped, although during the last 20 km from the terminus, the cross-profile of the main trough becomes non-uniform. A series of distinct overdeepenings, representing the lowest bed elevations in the catchment at up to 1625 m below sea level, are visible on the northern margin of the channel and offset the cross-profile here.

5.1.2 Basal Drag

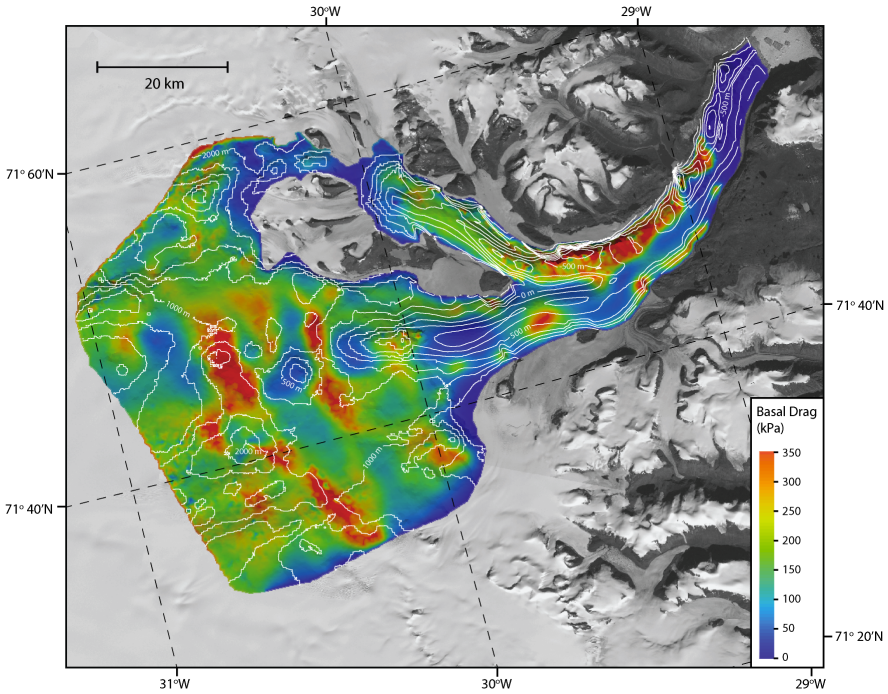

Figure 5.2: Map of modelled basal drag for Daugaard-Jensen Gletscher, overlaid on a RADARSAT-1 image mosaic. Bed topography is represented by 250 m contours in white.

The modelled basal drag illustrates a generally sticky bed beneath Daugard-Jensen Gletscher (Fig. 5.2), with basal drag reaching as high as 350 kPa in some locations. The high inland plateau surface is dominated by a number of discrete, elongated sticky spots, which appear to be orientated transverse to the general flow direction. In many cases, these areas lie adjacent to regions of much lower basal drag (<50 kPa) although these regions are more irregular in shape. Interestingly, the location of these sticky and non-sticky spots on the plateau appears to coincide superficially with local peaks and depressions in the bed topography respectively. Despite these more extreme values, the majority of the plateau still exerts a drag in the range of 150 – 200 kPa.

In the troughs, two interesting features are evident. Firstly, the smaller, northerly trough, where ice is both shallower and slower flowing, appears to be more sticky than the southerly trough, which is occupied by thicker and faster-flowing ice. Average drag in the northerly trough is 150 – 200 kPa, whilst in the south generally less than 150 kPa. The stickiness in the northerly trough continues into the main trough after the two troughs converge. Basal drag increases as ice flows over the sequence of overdeepenings, offset from the centre of the main channel. The second feature occurs approximately 10 km from the terminus. Here, basal drag rapidly decreases to less than 10 kPa across the entire width of the glacier and continues to remain low through to the terminus. This rapid reduction in drag approximately accompanies the transition of ice to the fastest flow speeds across the catchment.

Two patterns therefore emerge: high/low basal drag with peaks/depressions in the bed topography, and high/low basal drag with slow/fast ice flow. To investigate these relationships further, this data was sampled along a series of transects, the results of which are illustrated in Figure 5.3. Across the tranverse transects, the relationship is ambiguous. Furthest inland on transect A, basal drag appears to loosely correlate with local changes in bed elevation. For example, a clear decrease in basal drag by 100 kPa occurs at 25 – 30 km where the bed elevation drops by almost 700 m. However, either side of this depression, the relationship less evident. For transect B, a clearer association in visible, but it reveals the opposite to what occurs on transect A and here, basal drag increases by 100 kPa across the inception of the southerly trough, which represents a decrease in elevation by almost 1000 m. The association with velocity is less obvious for both of these transects and

appears to correlate more closely with bed topography than the magnitude of basal drag. Conversely for transects C and D, which are aligned with the glacier flow, a more noticeable relationship arises. Both transects agree strongly with the pattern seen on transect A, whereby basal drag increases and decreases with rises and depressions in the basal topography. This relationship appears to be more sensitive along transect D, which tracks ice entering from the stickier, northerly trough. Some exceptions are seen close to the terminus, where basal drag rapidly drops to less than 10 kPa whilst the bed topography rises. Velocity, which generally correlates poorly across both of these transects, rapidly increases concomitantly with the decrease in basal drag towards the terminus however.

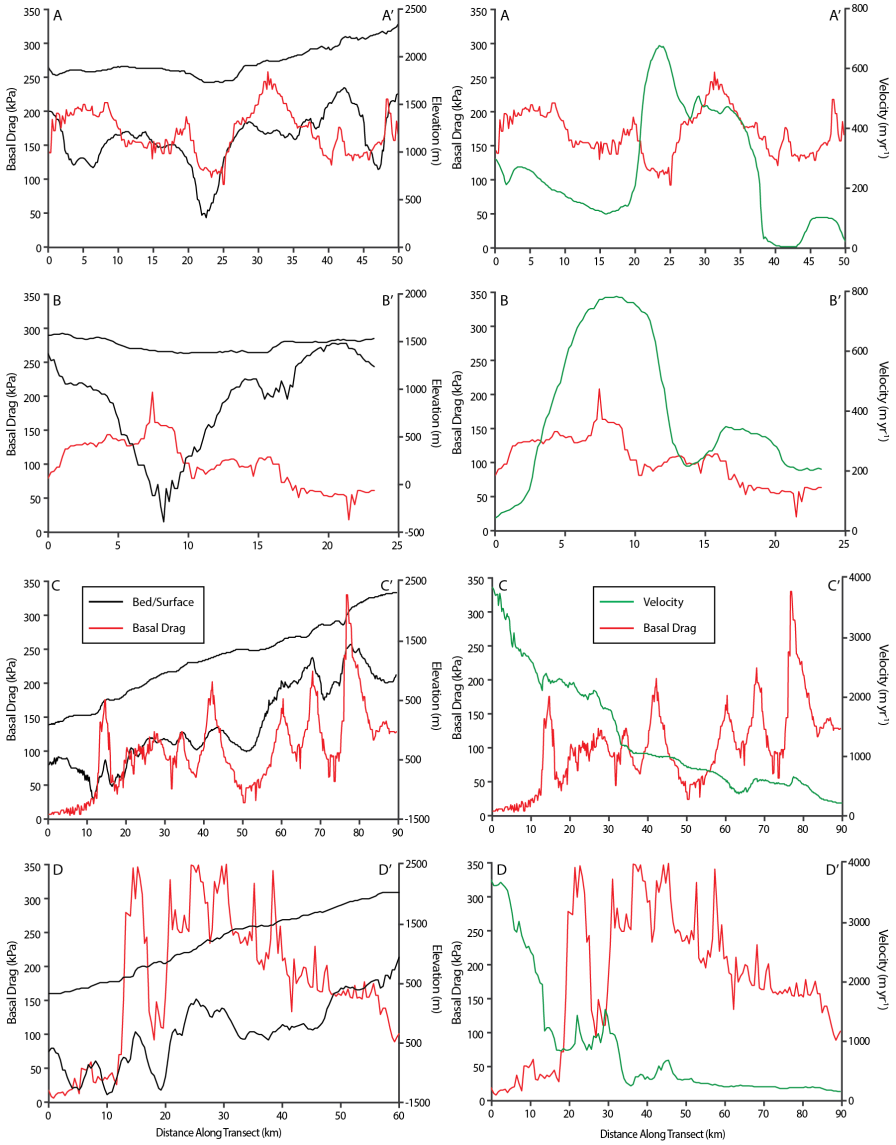

Figure 5.3: Comparison of basal drag (red) along 4 transects at Daugaard-Jensen Gletscher to bed and surface elevation (black) and velocity (green).

5.2 Academy Gletscher & Hagen Brae

5.2.1 Flow and Setting

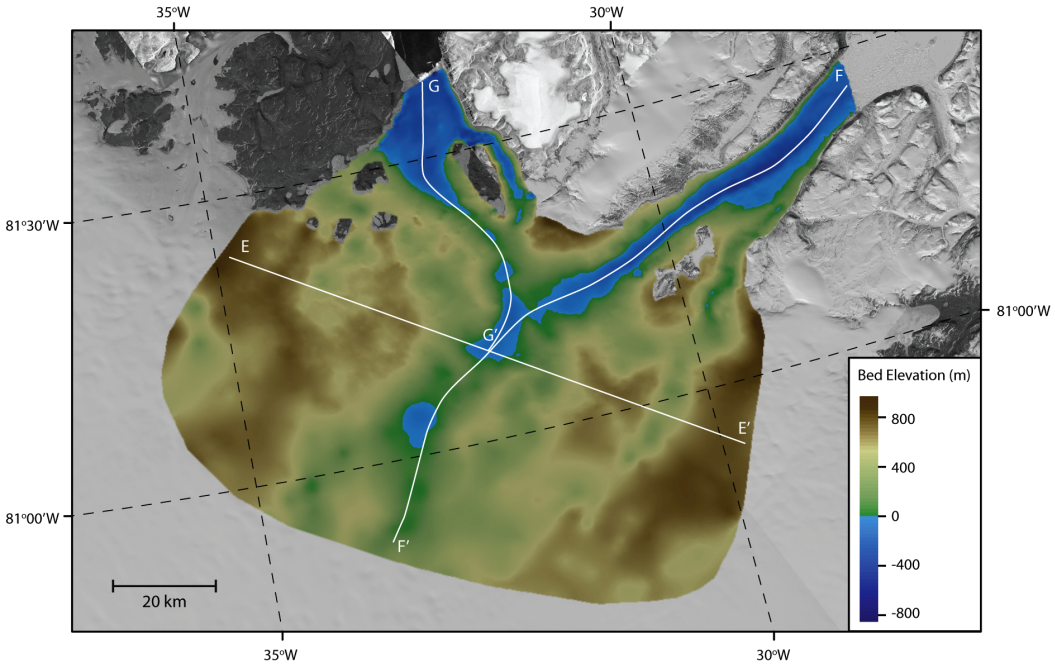

Figure 5.4: Map of bed topography for Academy Gletscher and Hagen Brae, derived from mass conservation and inland interpolation, overlaid on a RADARSAT-1 image mosaic. White lines illustrate locations of transects analysed in Figure 5.6.

The Academy Gletscher and Hagen Brae catchment (Fig. 5.4) is dominated by a 20 – 40 km wide channel, which is orientated in a northeasterly direction and extends into the interior. In elevation it is close to sea level or just below, and its location is consistent with faster surface ice velocities. The channel is bordered by higher terrain to the east and west, which reaches elevations of over 800 m above sea level in places, and is characterised by regions of slower flow. Some smaller channels (<10 km width), particularly in the east towards Hagen Brae, are incised into this higher ground however, concomitant with localised increases in velocity. The main central channel then bifurcates, at which point ice flows either into Academy Gletscher or Hagen Brae. The majority of the Academy Gletscher channel is below sea level, although the cross-profile shows more constant depth at around 400 m below sea level. Conversely to the east, Hagen Brae is comprised of a deeper channel, which reaches elevations of 800 m below sea level. This accompanies generally faster velocities here compared to Academy Gletscher. For both outlets, ice is deflected around nunataks, which, particularly in the case of Hagen Brae, appears to coincide with a local increase in velocity.

5.2.2 Basal Drag

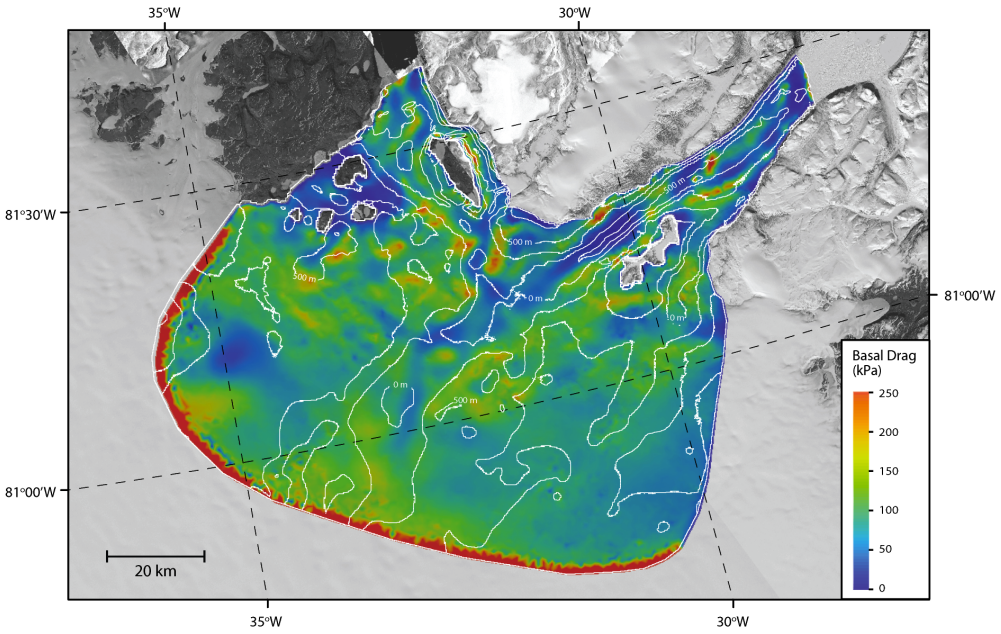

Figure 5.5: Map of modelled basal drag for Academy Gletscher and Hagen Brae, overlaid on a RADARSAT-1 image mosaic. Bed topography is represented by 250 m contours in white.

The modelled basal drag (Fig. 5.5) is generally lower compared to Daugaard-Jensen Gletscher, with an average drag of 100 kPa across the entire catchment. The central channel predominantly coincides with regions of lower (<75 kPa) basal drag, bordered by regions of higher (100-150 kPa) drag coincident with higher terrain. There are however a number of exceptions to this, and many areas of higher drag encroach into the channel. As such, a connected network of low basal drag regions within the overall channel is visible. Superimposed on the higher terrain are discrete sticky spots, where basal drag reaches 200-250 kPa. Some of these are elongated, but no consistent orientation is evident. After the main central channel bifurcates, the pattern of basal drag is less clear. There appears to be the same relationship between bed elevation and basal drag, however the terminus regions of both glaciers reveal a series of elongated sticky spots aligned with the flow direction. At Hagen Brae, basal drag also increases as ice flows around the 15 km long nunatak. The high drag seen at the south of the catchment is related to the inflow boundary condition in the model.

Since similar relationships between basal drag, velocity and bed elevation are again seen here, the connection is re-examined across 3 transects (Fig. 5.6). Unlike

Daugaard-Jensen Gletscher, the basal drag profile across the transverse transect E closely resembles the bed topography, lending further support for the relationship between drag and local changes in elevation. A poorer association is seen with velocity, although the drop in basal drag over the central channel matches the fastest flow speeds across the transect. Along transect F, which tracks ice flow into Academy Gletscher, the same connection with bed topography is seen. For example, at 30 – 40 km from the terminus, a 200 m high bedrock rise more than doubles the basal drag. The main exception to this trend is a rise in basal drag at the terminus by 40 kPa. Bed elevation here remains constant however the velocity approximately doubles. For transect G, which follows the Hagen Brae channel, basal drag appears particularly sensitive to small changes in bed elevation. Two large spikes in basal drag between 20 and 50 km from the terminus reflect neither bed topography or velocity. However, Figure 5.4 illustrates that this point represents the passage of ice through a pinning point generated by the nunatak and the coastal topography.

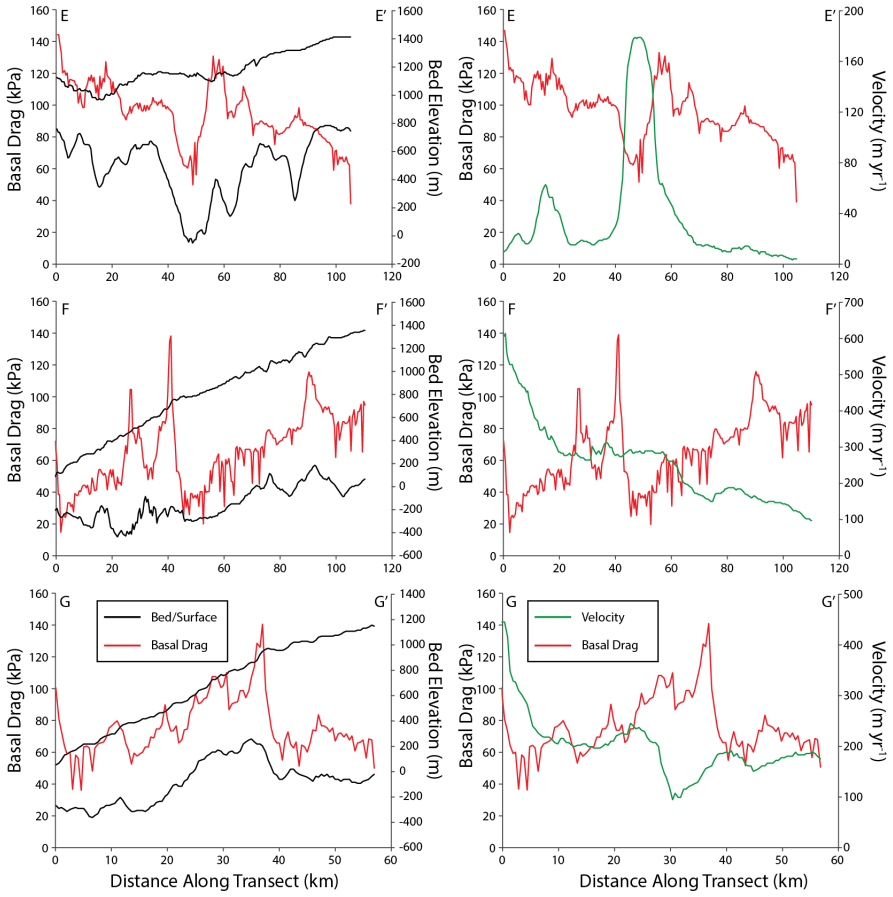

Figure 5.6: Comparison of basal drag (red) at Academy Gletscher and Hagen Brae along 3 transects to bed and surface elevation (black) and velocity (green).

5.3 Humboldt Gletscher

5.3.1 Flow and Setting

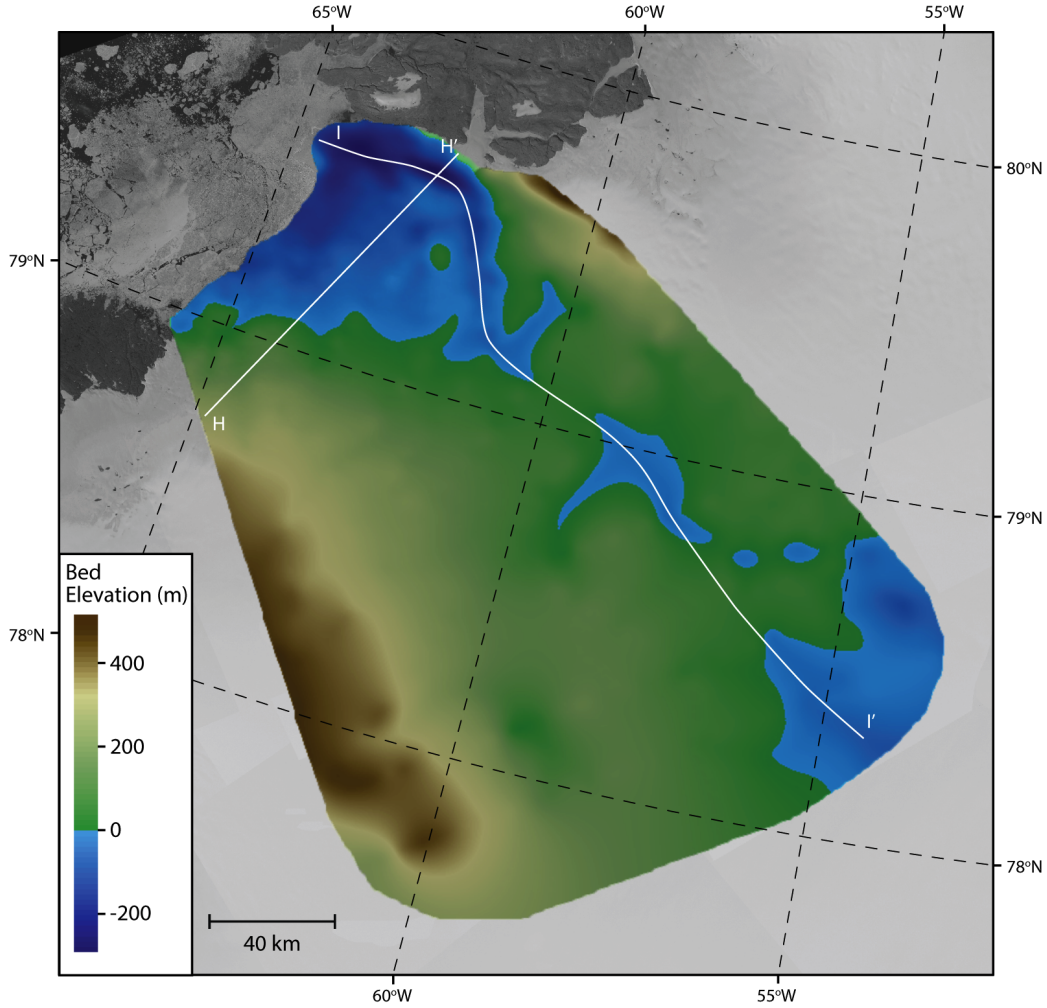

Figure 5.7: Map of bed topography for Humboldt Gletscher, derived from inland interpolation, overlaid on a RADARSAT-1 image mosaic. White lines illustrate locations of transects analysed in Figure 5.9.

Despite having the largest calving front of all glaciers in Greenland at 90 km, the bed topography of Humboldt Gletscher appears to be the least dramatic, however it has the largest area out of all the study sites residing below sea level at 4781 km^2 (Fig. 5.7). Bed elevations for most of the catchment range from 100 m below sea level to 200 m above sea level with an average of 131 m. This increases towards the westerly margin, consistent with the approach to mountainous ice-free terrain. Within 40 km of the terminus, the deepest elevations are found. Across the calving front, bed elevations are approximately 50 – 150 m below sea level, however at the northeastern margin of the catchment, a deep trough extends some 50 km inland

from the terminus. Here, elevations are depressed to about 220 m below sea level, and the fastest flow velocities are observed at 660 m yr^{-1}.

5.3.2 Basal Drag

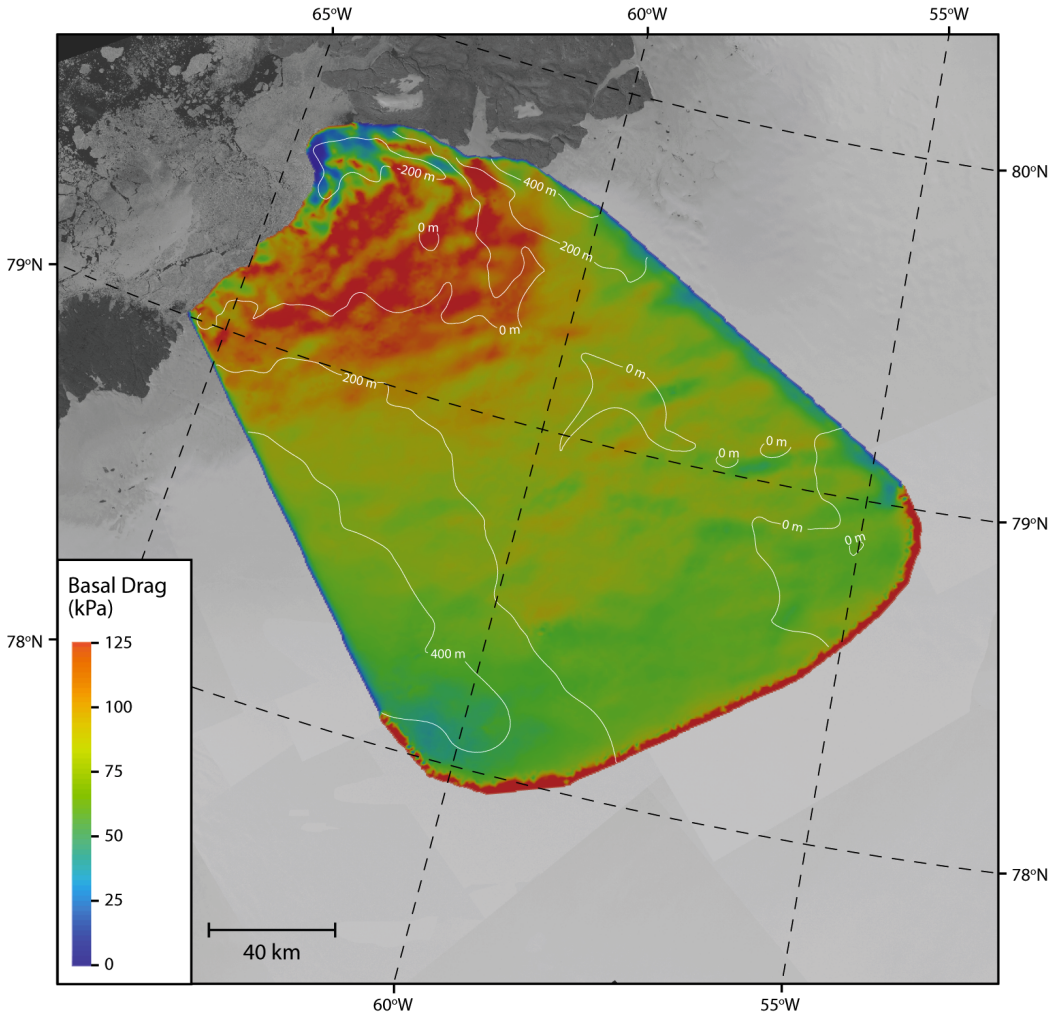

Figure 5.8: Map of modelled basal drag for Humboldt Gletscher, overlaid on a RADARSAT-1 image mosaic. Bed topography is represented by 250 m contours in white.

The model also reveals that the bed is the least sticky of the catchments, with a peak basal drag of 125 kPa (Fig. 5.8). The majority of this drag is focused in a large sticky spot, which stretches across the catchment behind the terminus and extends 40 – 60 km inland. Closer to the northerly margin, this sticky spot becomes more discontinuous, and transforms into a series of elongated ridges aligned parallel to the ice flow direction. A region of low (<25 kPa) basal drag is seen within 5 km of the terminus, coincident with the fastest flow speeds and

the deepest bed elevations. Moderate basal drag values (50-80 kPa) are visible inland, progressively decreasing towards the boundary of the model domain. The region of high basal drag at the innermost boundary is again related to the inflow boundary condition imposed in the model.

To explore the nature of this sticky spot, two transects were placed across this region in both longitudinal and transverse orientations (Fig. 5.9). Transect H, orientated transversely, highlights consistent ice thickness across the transect, but a descent in topography towards the East. The basal drag appears not to be affected by this, however it does locally decrease in the deep trough on the northeastern margin. Along transect I, orientated parallel to ice flow, basal drag is approximately constant between 150 and 270 km from the terminus. Ice thickness then markedly decreases, concomitant with an initial increase in basal drag from 75 – 120 kPa, followed by a decrease to 50 kPa. The final decrease in drag correlates with a rapid increase in velocity.

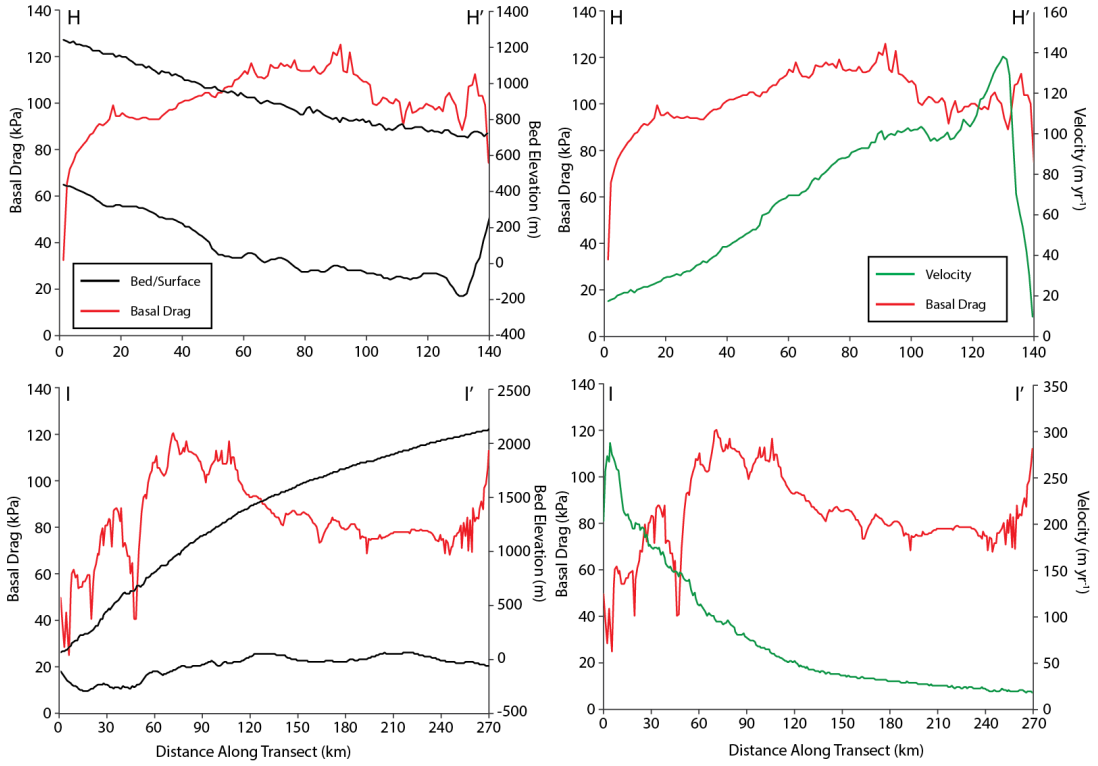

Figure 5.9: Comparison of basal drag (red) at Humboldt Gletscher along 2 transects to bed and surface elevation (black) and velocity (green).

5.4 Summary of Key Results

Table 5.1: Summary of key results in terms of flow, setting and basal boundary condition. Terminus velocities were calculated from the MEaSUREs dataset with the published uncertainty estimate. Annual discharge was calculated from the bed topography derived in this study and the MEaSUREs velocity data. A conservative uncertainty of 50 m was applied to the bed topography statistics due to the unfocused nature of the flightline data, and the known issues with radar sounding in the terminus regions. Uncertainty in inland extent and area is based on bed map resolution (<300 m). Uncertainty in average basal drag is one standard deviation of the mean.

	Daugaard-Jensen Gletscher	Academy Gletscher & Hagen Brae	Humboldt Gletscher
Flow			
Terminus velocity (m yr^{-1})	3200 ± 10	850 ± 10	660 ± 10
Annual discharge (km^3 yr^{-1})	12.9	2.35	3.63
Setting			
Max ice thickness (m)	2176 ± 50	1498 ± 50	2249 ± 50
Max bed elevation ASL (m)	2228 ± 50	981 ± 50	584 ± 50
Min bed elevation BSL (m)	-1625 ± 50	-982 ± 50	-312 ± 50
Average bed elevation (m)	900 ± 642	402 ± 280	131 ± 163
Inland extent BSL (km)	64 ± 0.3	89 ± 0.3	105 ± 0.3
Inland area BSL (km^2)	275 ± 0.09	768 ± 0.09	4781 ± 0.09
Basal Boundary Condition			
Max basal drag (kPa)	349	242	124
Average basal drag (kPa)	148 ± 96	82 ± 39	76 ± 20

Chapter 6

Discussion

The inherent difficulty with observing conditions at the bed means that the use of surface measurements to infer characteristics of the bed topography and bed conditions, as shown in this study, is extremely valuable. In this chapter, the accuracy of the results is evaluated by comparing data to datasets from similar studies. The implications of the results from each study site are then discussed, with a focus on ice dynamics and the future stability of these glaciers. Finally, some of the limitations of this methodology are acknowledged, leading onto future research directions outlined briefly in the next and final chapter.

6.1 Error Assessment

The nature of this investigation means that there is a close coupling between the derived bed topographies and the inversion process. As such, errors in the bed topography will be transferred across to the inversion, and so recognising the accuracy of the input data is a necessary step before one can interpret the results. To minimise the errors between the two, both methodologies made use of the latest datasets, which allowed both procedures to be completed at high spatial resolutions ($\leq$ 300 m). Furthermore, where possible, data was used from the same year to ensure consistency. The accuracy of the bed topographies is first analysed, followed by the inversion results.

6.1.1 Bed Quality

Bed topographies were derived from a combination of a novel mass conservation method, which places physical constraints on ice flow necessary for resolving dy-

namic outlet glacier topographies, and a geostatistical method for inland areas, which ensures sensible bed topographies are produced by enforcing water drainage. Each study site is now evaluated in turn, with respect to raw flightline measurements. Results are also compared to the latest ice sheet scale bed DEM by Bamber et al. [2013]. A conservative uncertainty estimate of 50 m is applied to the original ice thickness measurements due to the unfocused nature of the GrOGG data, the presence of heavy crevassing, and observed surface melting and ponding at all study sites.

6.1.1.1 Daugaard-Jensen Gletscher

The most inland transect, A, shows generally very good agreement with the other two datasets, as illustrated in Figure 6.1. At this location, the bed topography in this study was derived using the Topogrid function, and clearly it predicts accurately in this region, capturing both gentle and extreme bed topography very precisely. The Bamber et al. [2013] product generally correlates well, although deviates in the more gentle terrain by up to 200 m from the raw flightline points. Since their dataset employed the GrOGG data as well, the differences may be simply due to the spatial resolution of their product (1 km), although in addition, ordinary kriging is sensitive to correct optimisation of the semivariogram, which is difficult to achieve consistently over large spatial scales. At the inception of the more southerly trough, transect B also shows good agreement between the results of this study and the original flightline points, with the exception of just 1 point. Since this transect lies close to the boundary between bed topography derived from the Topogrid function and bed topography derived from mass conservation, the anomaly may be due to the integration process. However, radar sounding is prone to scatter in regions of more dramatic topography, as evidenced here, and so the error may come from the original flightline point. The Bamber et al. [2013] DEM also shows larger differences here, likely due to resolution rather than methodology because of the short length of this transect.

Transect C, which tracks the main trough and southerly tributary, shows discrepancies between the other two datasets when within 50 km of the terminus. There are several reasons for this, such as heavy crevassing and steep fjord topography which will have undoubtedly affected the ice thickness measurements in this area. Some erroneous artefacts clearly exist in the Bamber et al. [2013] DEM at 30 km and 15 km. Further inland, the datasets align well, and fjord inception is captured

precisely by all 3 datasets. Transect D, which tracks the main trough and northerly tributary shows that this study find deeper bed closer to the terminus. Whilst the lower resolution of the Bamber et al. [2013] dataset may average out some of the dramatic topography, comparison to available flight line data inland suggests that this study is perhaps more at fault. It is likely that errors are introduced by 'extra' mass input in this tributary, which drains a number of small glaciers from a mountainous region, and therefore the fluxgate is less accurate here. Further errors may be introduced by the velocity data, if, for example, the measured velocity is slower than in reality, then the mass conservation method will calculate a deeper bed than in reality.

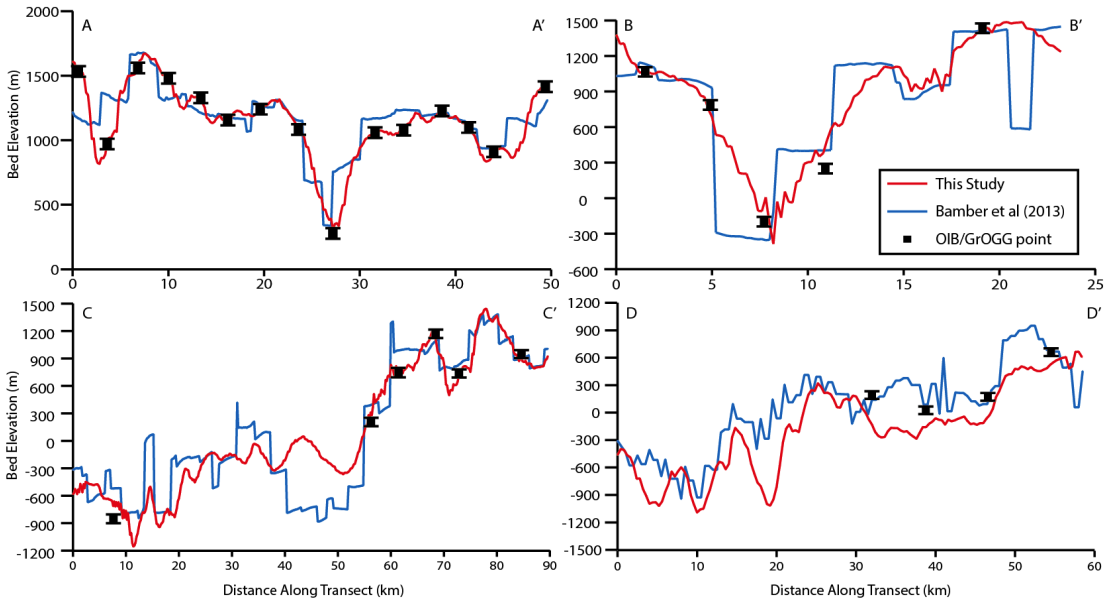

Figure 6.1: Comparison of bed elevation calculated in this study (red) to raw flightline values (black boxes) and Bamber et al. [2013] product (blue) across 4 transects at Daugaard-Jensen Gletscher. Error bars on raw flightline data are conservative at 50 m, due to the unfocused nature of the data and known issues with surveying outlet glacier regions.

6.1.1.2 Academy Gletscher & Hagen Brae

Along the transverse transect, E, there is generally good agreement between all three datasets, especially in regions of steep topography (Fig. 6.2). The Bamber et al. [2013] dataset appears to overestimate the magnitude of some of the changes in topography, however where original ice thickness measurements are present, both this study and Bamber et al. [2013] are within the uncertainty of the flight line data. The greatest discrepancy between the datasets is seen along transect F

which tracks ice flowing into Academy Gletscher. Greater than 20 km inland, the Topogrid function captures a rise in the bed topography that the Bamber et al. [2013] product does not. The length of the transect suggests that resolution is unlikely to be the cause, but perhaps the semivariogram was not correctly optimised for this region. Aside from the steep rise in topography at 20-40 km along the transect, this study appears to agree well with the results of Bamber et al. [2013], but less so with raw flight line data. This suggests either consistent error in both methodologies, erroneous flight line data, or infers bed topography too dramatic to be captured by either this study or that of Bamber et al. [2013]. The close agreement between this study and Bamber et al. [2013] suggests the original flight line data is at fault. Similar patterns of bed topography are replicated by this study and the Bamber et al. [2013] DEM along transect G, which tracks ice flowing into Hagen Brae. Small deviations occur from raw flight line data. The two most likely reasons for this are the generally slower velocities on this glacier, compared to Daugaard-Jensen Gletscher. This means that the uncertainty in the velocity data forms a higher percentage of the total, and the mass conservation method is particularly sensitive to this. This is reflected in the greater deviation from the original flight line data inland where velocities are even slower. In addition, the airborne survey here had greater spacing between flight tracks than at Daugaard-Jensen Gletscher, and so there are comparatively fewer data points to constrain the gridding process.

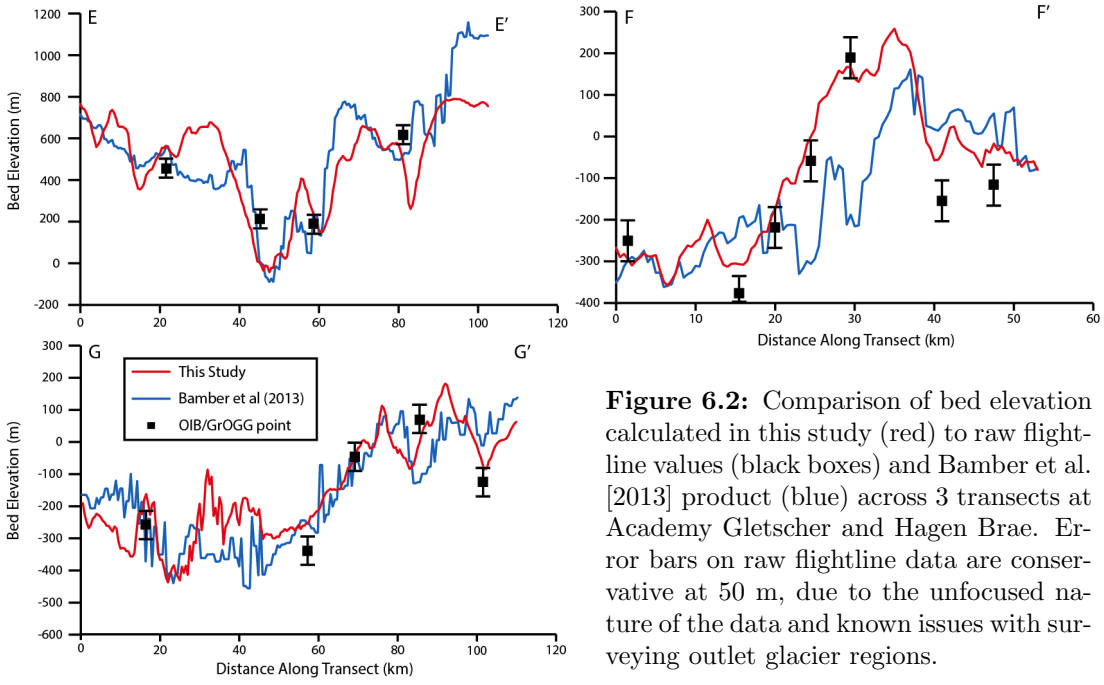

Figure 6.2: Comparison of bed elevation calculated in this study (red) to raw flightline values (black boxes) and Bamber et al. [2013] product (blue) across 3 transects at Academy Gletscher and Hagen Brae. Error bars on raw flightline data are conservative at 50 m, due to the unfocused nature of the data and known issues with surveying outlet glacier regions.

6.1.1.3 Humboldt Gletscher

Humboldt Gletscher highlights the strength of the Topogrid function, which predicts very accurately across both transects, compared to the Bamber et al. [2013] result (Fig. 6.3). Across transect H, the Bamber et al. [2013] drops to very low elevations towards the east, which suggests that it is not correctly capturing the ice free area that separates the catchment from the adjacent Petermann glacier. Synthetic data was generated over ice-free terrain in this study to achieve this. For the longitudinal transect I, the Bamber et al. [2013] DEM deviates significantly from both this study and raw flight line data within 140 km of the terminus. An erroneous artefact then causes a step in the Bamber et al. [2013] DEM and the 3 datasets agree more closely for the remaining length of the transect inland. This discovery highlights the benefits of the Topogrid function over the semivariogram-dependent kriging process used by Bamber et al. [2013]. Despite being able to handle steep topographies such as in the interior to the Academy Gletscher and Hagen Brae catchment, the highest accuracy here suggests that the Topogrid function is most accurate over more gentle topography.

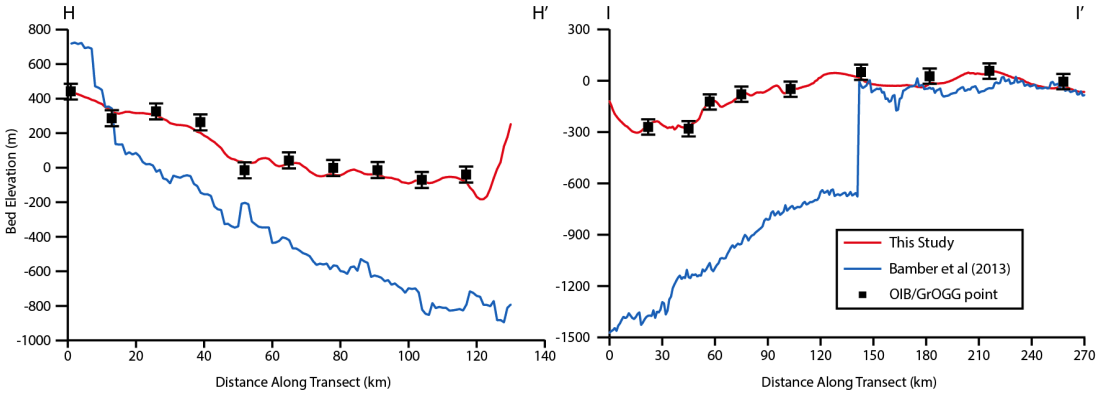

Figure 6.3: Comparison of bed elevation calculated in this study (red) to raw flightline values (black boxes) and Bamber et al. [2013] product (blue) across 2 transects at Humboldt Gletscher. Error bars on raw flightline data are conservative at 50 m, due to the unfocused nature of the data and known issues with surveying outlet glacier regions.

6.1.2 Basal Drag Quality

To assess the quality of the inversion results, the horizontal components of the modelled velocities were compared to the observed surface velocities (Fig. 6.4). The absolute difference was first calculated to reveal where the general areas of error occurred. This was then converted to a percentage of the observed velocity,

so that the result were not skewed by faster velocities. For example, a higher absolute error is often seen near the terminus, but sometimes only because velocity values are larger here. In addition, percentage error maps were clipped to exclude areas where observed velocities are less than 10 m yr^{-1} since these errors lie within the uncertainty of the velocity dataset [Joughin et al., 2010].

For Daugaard-Jensen Gletscher, there appears to be large absolute errors close to terminus in the order of 1000 m yr^{-1}, and some additional discrepancies inland in the order of 500 m yr^{-1}, however these occur only very locally, representing in total just 7-8% of the model domain. When absolute error is converted to a percentage of the observed velocity (relative error), this difference is worth approximately 2% and therefore regarded as not significant. Nevertheless, the error is likely due to an incorrect viscosity near the terminus as shear-softening of the ice becomes more influential, and because the existence of a floating section is not accounted for by the model. Furthermore, observed velocities ignore the vertical velocity component in the ice flow, which may become important across the series of overdeepenings. Inland the model is sometimes prone to producing high basal drag values were velocities are low because this produces a very low gradient in the cost function [T. Zwinger, personal communication].

For Academy Gletscher and Hagen Brae, absolute velocity mismatch is only as high as 200 m yr^{-1}, however peak velocities are also lower here compared to Daugaard-Jensen Gletscher. The main sources of this discrepancy appears to be located on channel margins, suggesting that the vertical component of the velocity is again important here. When converted to relative error, absolute error is worth about 1% of the observed velocity, and so again not significant. The source of this error may be because of non-convergence in the minimisation of the cost function, often produced where the gradient of the cost function is low due to efficient minimisation in early iterations of the model [Gillet-Chaulet et al., 2012]. A notable area of the model domain is also within the 10 m yr^{-1} uncertainty of the velocity dataset.

Finally, at Humboldt Gletscher, absolute error is less than 50 m yr^{-1}, equating to about 2.5% error for most of the model domain. It appears that this rises towards the southwestern margin of the catchment, where velocities are lower and therefore more uncertain. A large portion of this area of the domain is within observed velocity uncertainty and therefore exluded.

The consistently low relative error at all study sites lends further support to the accuracy of the bed topographies. Since no free surface evolution was employed in the numerical model, the ice thickness between the surface and bed DEMs must correctly accommodate the mass flux prescribed by the surface velocity, otherwise large errors would be introduced.

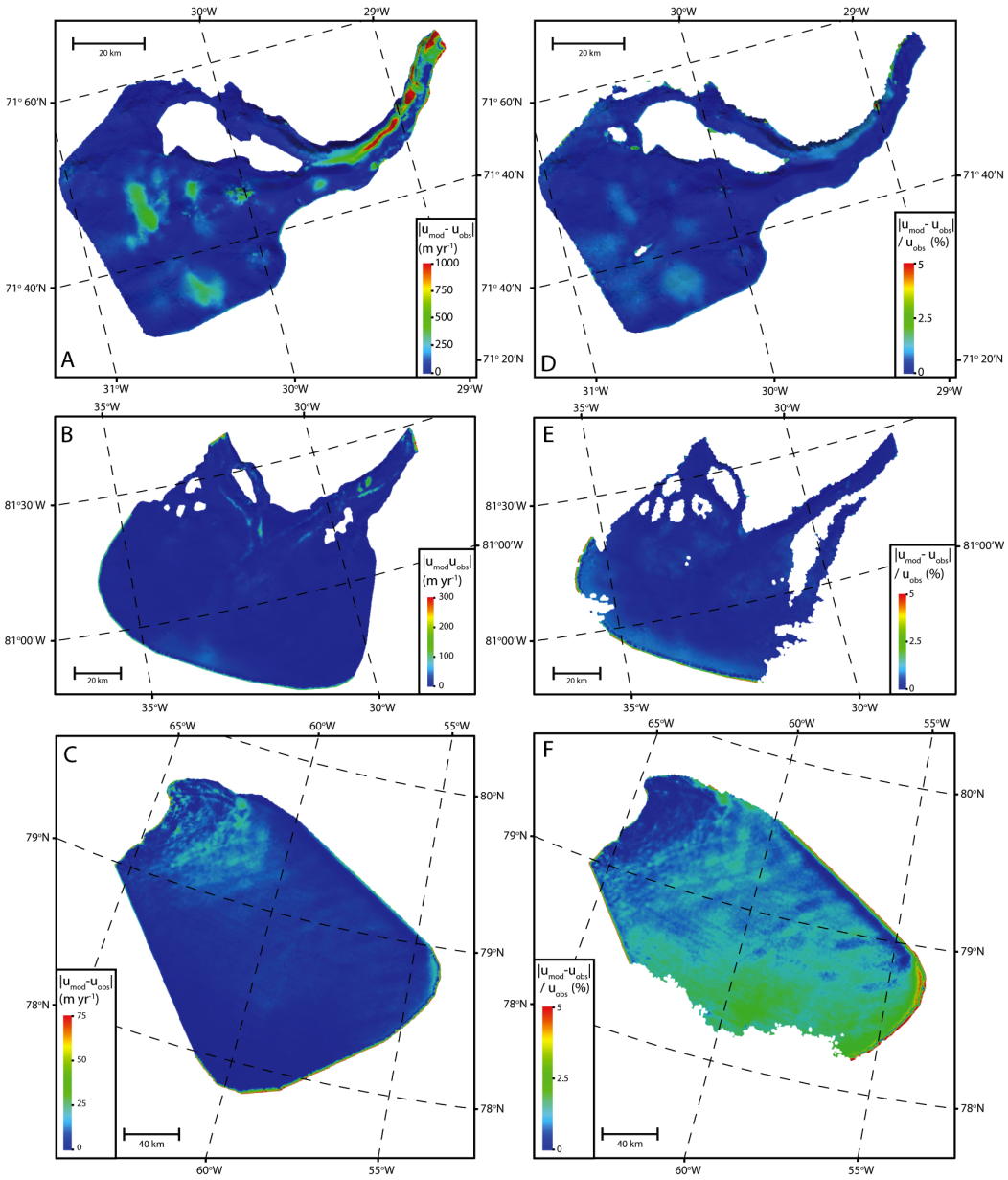

Figure 6.4: Absolute error, A-C, as $|u_{mod} - u_{obs}|$, and relative error, D-F, as $|u_{mod} - u_{obs}|/u_{obs}$ in modelled velocity from the inversions across the three study sites. Maps D-F are clipped to where u_{obs} is greater than 10 m yr^{-1}.

6.2 Inferences on Ice Dynamics

This study has analysed a selection of glaciers in northern Greenland. By deriving accurate and high-resolution bed topographies and modelling the drag at the base of these glaciers, a number of inferences can be made on their ice dynamics.

A consistent pattern is seen in the bed topography, whereby high terrain is dissected by deep channels. The presence of these channels is particularly obvious beneath the Daugaard-Jensen Gletscher and the Academy Gletscher and Hagen Brae catchments, however a less extensive channel is also observed towards the northeast margin of Humboldt Gletscher. The coincidence of these channels with fast flow suggests that they are glacial in origin rather than relict fluvial features, and this is further supported by their characteristic U-shaped cross-profile [Harbor, 1992]. More widespread analyses also confirm a similar trend at different latitudes in Greenland [Morlighem et al., 2014]. These channels often extend far inland, and therefore play an important role in channeling ice from the interior towards the margins. Indeed, the higher bed elevations seen in the interior of the Daugaard-Jensen Gletscher and the Academy Gletscher and Hagen Brae catchments still exhibit fast flow velocities, underscoring the impact of these deep channels in pulling ice from the interior. The presence of these channels may also reflect a change in local geology, as suggested by Swift et al. [2008] who note that geology and lithological strength has been a first-order control on the glacial modification of the East Greenland landscape, where a resistive Caledonian basement favours vertical incision and overdeepening rather than widening. The inception of these channels may also demonstrate the influence of surface topography on steering ice flow and locally enhancing erosion [Kessler et al., 2008], which would explain why Humboldt Gletscher does not exhibit such dramatic bed topography because it is poorly confined by surface topography.

Analysis of basal drag emphasises a strong relationship with the shape of the bed, whereby local depressions and high points in the bed topography consistently coincide with regions of higher and lower basal drag respectively. Previous research has shown that bed perturbations, with wavelengths similar to the ice thickness, are capable of creating form drag at the bed [e.g. Gudmundsson et al., 1998; Schoof, 2002]. Indeed for the inland areas at Daugaard-Jensen Gletscher, the location of low drag regions are located on the leeside of high drag regions (Fig. 6.5), and also

display a characteristic surface expression in the form of a stationary surface undulation followed by flow stripes depending on the local ice viscosity [Gudmundsson, 2003; De Rydt et al., 2013]. However, in many cases, these surface expressions are absent, and although this may in part be due to higher ice temperatures which suppress the surface form, it is equally possible that a second mechanism exists. Since the strongest correlation occurs when ice flow speeds are relatively high, it is possible that efficient glacial erosion is infilling local depressions in the bed topography with unconsolidated sediment, which deforms readily and therefore exerts only very low values of basal drag on the overlying ice. Indeed, Swift et al. [2002] note that inefficient, distributed hydrological systems, typical on the plateau, are poor at evacuating sediment compared to a channelised hydrological system. Furthermore, depressions in the bed topography locally suppress the efficiency of the subglacial drainage system [Cook and Swift, 2012], and Hooke and Pohjola [1994] suggest that depressions and overdeepenings may therefore act as storage pockets for till. Conversely, over local highs in the bed topography, any surface sediment will have been removed and ice will scour these regions, creating high basal drag, as observed at the study sites here.

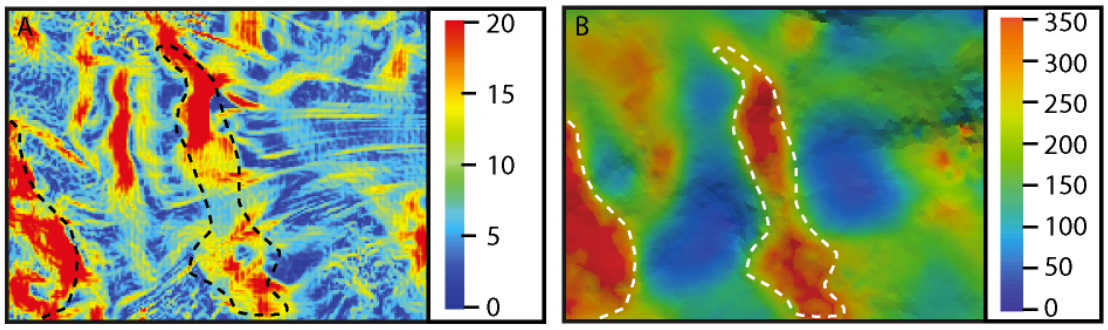

Figure 6.5: Relationship between surface slope in degrees (A) and basal drag in kPa (B) at the head of the southerly trough of Daugaard-Jensen Gletscher. White and black dashed lines indicate areas where high basal drag coincides with high surface slope due to the transmission of this drag to the surface. Flow stripes are also visible downflow.

This mechanism of sediment infill in topographic depressions may be highly influenced or indeed replaced by the morphology of the subglacial hydrological system. In some scenarios, water generated by pressure-melting, surface melting and frictional heating could collect in depressions at the bed and previous research has found bright radar reflectances over depressions in the bed, consistent with the accumulation of water in such locations [e.g. Siegert et al., 1996; Palmer et al., 2013]. Since basal melting is expected to be highest over the thickest ice, the closest interplay between water and sediment may be seen in these regions, where melting

of debris-rich basal ice is able to deposit soft sediment in topographic depressions in the bed. A combination of water and sediment may also act in the lower regions of the glaciers, closer to the terminus. In fact the rapid reduction in basal drag within the last 10 km of the terminus of Daugaard-Jensen Gletscher suggests partial or full flotation of the ice in this area. More widespread evidence for soft beds beneath these glaciers is provided at Academy Gletscher and Hagen Brae, where a series of elongated sticky spots aligned parallel to flow are visible near the termini of both glaciers. There is no correlation with bed topography for these occurrences and one would expect lower effective pressures at the bed closer to the termini. Therefore it is possible that these represent discontinuous till cover, or alternatively the presence of isolated bedrock bumps below the resolution of the bed DEM that have been streamlined by the flow of ice. Some analogies to the latter have been observed at Jakobshavn Isbrae further south [Jezek et al., 2011]. Unfortunately, the unavailability of focused airborne radar sounding data at the time of writing means that bed echo amplitudes cannot be examined to confirm either mechanism.

Some additional features of interest make some exceptions to this trend however. At Daugaard-Jensen Gletscher, the northerly tributary to the main trough displays higher drag than the larger, more southerly tributary. The northerly tributary drains a smaller area and is not directly fed from the plateau but originates in a mountainous region. Therefore the efficacy of either mechanism could be reduced, thus increasing the basal drag. Alternatively, since flow velocities are slower in this tributary, ice may be buttressed by the fast flowing ice entering the main trough from the southerly tributary. There is some support for this hypothesis in that a region of high basal drag is evident on the northerly margin of the main trough, in the same location as the sequence of overdeepenings, which would ordinarily be expected to collect sediment or water and locally reduce basal drag. Therefore, ice may be squeezed in this area by the faster-flowing ice from the south. At Academy Gletscher and Hagen Brae further north, regions of high basal drag are created as ice flows between fjord walls and nunataks. This demonstrates the effect of pinning points in creating basal drag as ice is slowed by lateral resistance. Finally, at Humboldt Gletscher, a large sticky spot exists behind the terminus. It is unlikely that this represents lateral stress transmitted across the glacier since the terminus is some 90 km wide. Instead, this may represent a local geological control, such as a transition to hard bedrock, or alternatively, if a soft bed dominates, a transition to strong, well-drained till which deforms less readily.

6.3 Implications for Future Stability

The results of this study generally imply that tidewater glaciers in northern Greenland will become increasingly unstable in future years. At all study sites, a significant area of the bed topography lies below sea level, and this often extends far inland. Since sea level strongly impacts the subglacial water pressure, future sea level rise will likely further decouple the ice from the bed, reducing resistance to flow. Long-term stabilisation of Daugaard-Jensen Gletscher is likely to only occur once ice has retreated some 70 km inland, and reaches the high plateau surface, where fjord inception strongly controls ice flow into the fjord [McIntyre, 1985]. Similarly for Humboldt Gletscher, which has a generally shallow bed at elevations close to sea level, a small rise in sea level will result in significant areas of the bed becoming fully submarine. Whilst ocean forcing of ice dynamics at these high latitudes is weaker due to the isolation from the warmest subtropical currents, there is evidence for some ice-ocean interaction [Enderlin and Howat, 2013]. The amplification of surface melting with projected warming and the subsequent delivery of this water to the bed will likely energise meltwater plumes at the ice fronts of the glaciers when it is then discharged subglacially across the grounding line.

6.4 Uncertainties and Limitations

Whilst a number of important implications arise from the results of this study, a number of uncertainties and limitations must be acknowledged.

The bed topographies were derived from unfocused GrOGG data and for the mass conservation part, from a single flux gate for each outlet glacier. This may have introduced errors into the bed topography, which remain uncorrected because only flux gate was used. The use of the GrOGG data however allowed significantly higher resolution bed topographies to be produced, particularly inland, than what would be possible with only OIB data. For the mass conservation method, more recent adaptations of this method have added the option of including all available flightline data to constrain the final product [Morlighem et al., 2013]. Whilst this would undoubtedly improve the accuracy, as Section 6.1.1 illustrates, the majority of the results were consistently within the uncertainty of the raw ice thickness values, suggesting that the latter is not an unacceptable limitation. The results were also consistently more accurate than the latest ice sheet scale product [Bamber

et al., 2013].

Inversions are sensitive to their input data, however analysis of the velocity mismatch showed very low percentage error for all study sites. In some locations, such as Daugaard-Jensen Gletscher, regions of stickiness may be over predicted by the model due to the more simplistic temperature assumptions, particularly the neglection of pressure-melting and geothermal flux in the heat budget of the model. Some of the velocity mismatch observed near the terminus regions could be rectified by allowing softer ice in these regions, which would in turn allow deformation more readily.

Chapter 7

Conclusions

Tidewater outlet glaciers in northern Greenland exhibit fast flow regimes, despite isolation from strong ocean forcing, which is responsible for large-scale changes at lower latitudes in Greenland. This suggests that conditions at the bed may play an important, and previously unknown role in regulating their flow. The aim of this research has been to assess conditions at the bed of several tidewater outlet glaciers in northern Greenland, by deriving new high-resolution bed DEMs and calculating basal drag using an inverse method. From the results of this study, several conclusions may be drawn.

(1) By combining a novel mass conservation method, which places physical constrains on ice dynamics, with an interpolation algorithm that ensures realistic hydrological pathways, the dramatic bed topography of outlet glaciers may be reconstructed with a vertical accuracy and spatial resolution superior to that of ice sheet scale products.

(2) These reconstructed bed topographies highlight that significant areas of the study sites lie close to, or below sea present level. They also reveal channels which are both deeper and extend further inland than previously thought. This implies that outlet glaciers in northern Greenland are vulnerable to future changes in climate and sea level, and may contribute substantially to sea level rise through nearly unrestricted retreat inland.

(3) 3D inversions using the Elmer/Ice model reveal that basal drag is spatially variable across these glaciers but is closely coupled with local elevation changes in the bed topography. This likely reflects the influence of form drag or the accumula-

tion of water and soft, deformable sediment beneath these glaciers, which provides little resistance to flow. A future increase in surface melting and the delivery of this water to the bed will exacerbate this trend and may destabilise these glaciers in future.

(4) The results underscore the need for further direct and indirect observations of the bed in order to better constrain the future flow of glaciers at all latitudes in Greenland.

7.1 Future Study

Considering these conclusions, several avenues for future research are now outlined. Whilst bed topographies have recently been resolved in detail for a number of outlet glaciers in Greenland [e.g. Morlighem et al., 2014], relatively few studies have applied inverse methods in full-stokes models to recreate conditions at the bed with accuracy. This in itself remains a major goal in glaciology.

With regards to this study, the inclusion of a more robust temperature relationship, which accounts for changes in viscosity near the terminus related to shear-softening of ice, and the introduction of meltwater at the base as a consequence of pressure-melting and geothermal heating, would refine absolute values of basal drag at these glaciers. Nevertheless, a more simple viscosity model, as applied here, yields important insight into the spatial pattern of basal drag.

References

Abdalati, W., Krabill, W., Frederick, E., Manizade, S., Martin, C., Sonntag, J., Swift, R., Thomas, R., Wright, W., and Yungel, J. (2001). Outlet glacier and margin elevation changes: Near-coastal thinning of the Greenland ice sheet. *Journal of Geophysical Research: Atmospheres*, 106(D24):33729–33741.

Alley, R., Blankenship, D., Bentley, C., and Rooney, S. (1986). Deformation of till beneath Ice Stream B, West Antarctica. *Nature*, 322(6074):57–59.

Anklin, M., Bales, R., Mosley-Thompson, E., and Steffen, K. (1998). Annual accumulation at two sites in northwest Greenland during recent centuries. *Journal of Geophysical Research: Atmospheres*, 103(D22):28775–28783.

Bamber, J. L., Ekholm, S., and Krabill, W. (2001a). A new, high-resolution digital elevation model of Greenland fully validated with airborne laser altimeter data. *Journal of Geophysical Research: Solid Earth*, 106(B4):6733–6745.

Bamber, J. L., Griggs, J. A., Hurkmans, R. T. W. L., Dowdeswell, J. A., Gogineni, S. P., Howat, I., Mouginot, J., Paden, J., Palmer, S., Rignot, E., and Steinhage, D. (2013). A New Bed Elevation Dataset for Greenland. *The Cryosphere*, 7:499–510.

Bamber, J. L., Layberry, R., and Gogineni, S. P. (2001b). A new ice thickness and bed data set for the Greenland ice sheet: 2. Measurement, data reduction, and errors. *Journal of Geophysical Research: Solid Earth*, 106(D24):33773–33780.

Bartholomew, I., Nienow, P., Mair, D., Hubbard, A., King, M., and Sole, A. (2010). Seasonal evolution of subglacial drainage and acceleration in a Greenland outlet glacier. *Nature Geoscience*, 3(6):408–411.

Bell, R. (2008). The role of subglacial water in ice-sheet mass balance. *Nature Geoscience*, 1(5):297–304.

Benn, D. and Evans, D. (2010). *Glaciers and Glaciation*. Hodder Education: Oxford, UK.

Benn, D., Hulton, N., and Mottram, R. (2007). 'Calving laws', 'sliding laws' and the stability of tidewater glaciers. *Annals of Glaciology*, 46:123–130.

Bevan, S., Murray, T., Luckman, A., Hanna, E., and Huybrechts, P. (2012). Stable dynamics in a Greenland tidewater glacier over 26 years despite reported thinning. *Annals of Glaciology*, 53(60):241–248.

Bindschadler, R., Jezek, K., and Crawford, J. (1987). Glaciological Investigations Using the Synthetic Aperture Radar Imaging System. *Annals of Glaciology*, 9:11–19.

Block, A. and Bell, R. (2011). Geophysical evidence for soft bed sliding at Jakobshavn Isbrae, West Greenland. *The Cryosphere Discuss*, 5:339–366.

Boulton, G. (1986). Geophysics: A paradigm shift in glaciology? *Nature*, 322(6074):18.

Boulton, G. and Hindmarsh, R. (1987). Sediment deformation beneath glaciers: Rheology and geophysical consequences. *Journal of Geophysical Research: Solid Earth*, 92(B9):9059–9082.

Boulton, G. and Jones, A. (1979). Stablity of temperate ice caps and ice sheets resting on beds of deformable sediment. *Journal of Glaciology*, 24(90):29–43.

Box, J., Bromwich, D. H., Veenhuis, B., Bai, L.-E., Stroeve, J., Rogers, J., Steffen, K., Haran, T., and Wang, S.-H. (2006). Greenland Ice Sheet Surface Mass Balance Variability (1988-2004) from Calibrated Polar MM5 Output. *Journal of Climate*, 19(12):2783–2800.

Box, J. and Decker, D. (2011). Greenland marine-terminating glacier area changes: 2000-2010. *Annals of Glaciology*, 52(59):91–98.

Budd, W., Keage, P., and Blundy, N. (1979). Empirical studies of ice sliding. *Journal of Glaciology*, 23(89):157–170.

Christoffersen, P., O'Leary, M., van Angelen, J. H., and van den Broeke, M. R. (2012). Partitioning effects from ocean and atmosphere on the calving stability of Kangerdlugssuaq Glacier, East Greenland. *Annals of Glaciology*, 53(60):249–256.

Clarke, G. (2005). Subglacial Processes. *Annual Reviews of Earth and Planetary Science*, 33(1):247–276.

Cook, S. and Swift, D. (2012). Subglacial basins: Their origin and importance in glacial systems and landscapes. *Earth-Science Reviews*, 115(4):332–372.

Cuffey, K., Conway, H., Gades, A., Hallet, B., Raymond, C., and Whitlow, S. (2000). Deformation properties of subfreezing glacier ice: Role of crystal size, chemical impurities, and rock particles inferred from in situ measurements. *Journal of Geophysical Research: Solid Earth*, 105(B12):27895–27915.

Cuffey, K., Conway, H., Hallet, B., Gades, A., and Raymond, C. (1999). Interfacial water in polar glaciers and glacier sliding at -17°C. *Geophysical Research Letters*, 26(6):751–754.

Cuffey, K. and Paterson, W. (2010). *Physics of Glaciers*. Academic Press: Waltham, MA, USA.

Davies, W. and Krinsley, D. (1962). The recent regimen of the ice cap margin in North Greenland. *International Association of Scientific Hydrology Publication*, 58:119–130.

De Rydt, J., Gudmundsson, G., Corr, H., and Christoffersen, P. (2013). Surface undulations of Antarctic ice streams tightly controlled by bedrock topography. *The Cryosphere*, 7:407–417.

Dowdeswell, J. A., Whittingdon, R., and Hodgkins, R. (1992). The sizes, frequencies, and freeboards of east greenland icebergs as observed using ship radar and sextant. *Journal of Geophysical Research: Oceans*, 97(C3):3515–3528.

Duval, P., Arnaud, L., Brissaud, O., Montagnat, M., and de la Chapella, S. (2000). Deformation and recrystallisation processes of ice from polar ice sheets. *Annals of Glaciology*, 30(1):83–87.

Ekström, G., Nettles, M., and Tsai, V. C. (2006). Seasonality and Increasing Frequency of Greenland Glacial Earthquakes. *Science*, 311(5768):1756–1758.

Enderlin, E. and Howat, I. (2013). Submarine melt rate estimates for floating termini of Greenland outlet glaciers (2000-2010). *Journal of Glaciology*, 59(213):67–75.

Enderlin, E., Howat, I., Jeong, S., Noh, M.-H., van Angelen, J. H., and van den Broeke, M. R. (2014). An improved mass budget for the Greenland Ice Sheet. *Geophysical Research Letters*, 41(3):866–872.

Engelhardt, H., Humphrey, N., Kamb, B., and Fahnestock, M. (1990). Physical Conditions at the Base of a Fast Moving Antarctic Ice Stream. *Science*, 248(4951):57–59.

Engelhardt, H. and Kamb, B. (1998). Basal sliding of Ice Stream B, West Antarctica. *Journal of Glaciology*, 44(147):223–230.

Ettema, J., van den Broeke, M. R., van Meijgaard, E., van de Berg, W. J., Bamber, J. L., Box, J., and Bales, R. (2009). Higher surface mass balance of the Greenland ice sheet revealed by high-resolution climate modelling. *Geophysical Research Letters*, 36(12):1–5.

Ettema, J., van den Broeke, M. R., van Meijgaard, E., van de Berg, W. J., Box, J., and Steffen, K. (2010). Climate of the Greenland ice sheet using a high-resolution climate model - Part 1: Evaluation. *The Cryosphere*, 4:511–527.

Fastook, J., Brecher, H., and Hughes, T. (1995). Derived Bedrock Elevations, Strains and Stresses from Measured Surface Elevations and Velocities - Jakobshavns Isbrae, Greenland. *Journal of Glaciology*, 41(137):161–173.

Fowler, A. (1981). A Theoretical Treatment of the Sliding of Glaciers in the Absence of Cavitation. *Philosophical Transactions of the Royal Society A*, 298(1445):637–681.

Fowler, A. (2011). Weertman, Lliboutry and the development of sliding theory. *Journal of Glaciology*, 56(200):965–972.

Fretwell, P., Pritchard, H., Vaughan, D. G., Bamber, J. L., Barrand, N., Bell, R., Bianchi, C., Bingham, R., Blankenship, D. D., Casassa, G., Catania, G., Callens, D., Conway, H., Cook, A., Corr, H. F. J., Damaske, D., Damm, V., Ferraccioli, F., Forsberg, R., Fujita, S., Furukawa, T., Gogineni, P., Griggs, J., Hamilton, G., Hindmarsh, R., Holmlund, P., Holt, J., Jacobel, R., Jenkins, A., Jokat, W., Jordan, T., King, E. C., Krabill, W., Riger-Kusk, M., Tinto, K., Langley, K., Leitchenkov, G., Luyendyk, B. P., Matsuoka, K., Nixdorf, U., Nogi, Y., Nost, O., Popov, S., Rignot, E., Rippin, D., Riviera, A., Ross, N., Siegert, M. J., Shibuya, K., Smith, A., Steinhage, D., Studinger, M., Sun, B., Thomas,

R., Tabacco, I., Welch, B., Young, D., Xiangbin, C., and Zirizzotti, A. (2013). Bedmap2: improved ice bed, surface and thickness datasets for Antarctica. *The Cryosphere*, 7:375–393.

Frey, P. and Alauzet, F. (2005). Anisotropic mesh adaptation for CFD computations. *Computer Methods in Applied Mechanics and Engineering*, 194(48-49):5068–5082.

Gagliardini, O., Cohen, D., Raback, P., and Zwinger, T. (2007). Finite-element modelling of subglacial cavities and related friction law. *Journal of Geophysical Research: Earth Surface*, 112(F2):1–11.

Gagliardini, O., Zwinger, T., Gillet-Chaulet, F., Durand, G., Favier, L., de Fleurian, B., Greve, R., Malinen, M., Martin, C., Raback, P., Ruokolainen, J., Sacchettini, M., Schafer, M., Seddik, H., and Thies, J. (2013). Capabilities and performance of Elmer/Ice, a new-generation ice sheet model. *Geoscientific Model Development*, 6:1299–1318.

Gilbert, J. and Lemaréchal, C. (1989). Some Numerical Experiments with Variable-Storage Quasi-Newton Algorithms. *Mathematical Programming*, 45(1-3):407–435.

Gillet-Chaulet, F., Gagliardini, O., Seddik, H., Nodet, M., Durand, G., Ritz, C., Zwinger, T., Greve, R., and Vaughan, D. (2012). Greenland ice sheet contribution to sea-level rise from a new-generation ice-sheet model. *The Cryosphere*, 6:1561–1576.

Glen, J. (1952). Experiments on the deformation of ice. *Journal of Glaciology*, 2(12):111–114.

Glen, J. (1953). Rate of Flow of Polycrystalline Ice. *Nature*, 172(4381):721–722.

Glen, J. (1955). The Creep of Polycrystalline Ice. *Proceedings of the Royal Society A*, 228(1175):519–538.

Gogineni, S. P., Tammana, D., Braaten, D., Leuschen, C., Akins, T., Legarsky, J., Kanagaratnam, P., Stiles, J., Allen, C., and Jezek, K. (2001). Coherent radar ice thickness measurements over the Greenland ice sheet. *Journal of Geophysical Research: Atmospheres*, 106(D24):33761–33772.

Goodman, D., Frost, H., and Ashby, M. (1981). The plasticity of polycrystalline ice. *Philosophical Magazine A*, 43(3):665–695.

Greve, R. (2005). Relation of measured basal temperatures and the spatial distribution of the geothermal heat flux for the Greenland ice sheet. *Annals of Glaciology*, 42(1):424–432.

Gudmundsson, G. (1997). Basal-flow characteristics of a non-linear flow sliding frictionless over strongly undulating bedrock. *Journal of Glaciology*, 43(143):80–89.

Gudmundsson, G. (2003). Transmission of basal variability to a glacier surface. *Journal of Geophysical Research: Solid Earth*, 108(B5):1–19.

Gudmundsson, G., Raymond, C., and Bindschadler, R. (1998). The origin and longevity of flow stripes on Antarctic ice streams. *Annals of Glaciology*, 27:145–152.

Hansen, P. (2001). *Computational Inverse Problems in Electrocardiology*, volume 5, chapter The L-curve and its use in the treatment of inverse problems. WIT Press: Southampton, UK.

Harbor, J. (1992). Numerical modelling of the development of U-shaped valleys by glacial erosion. *Geological Society of America Bulletin*, 104(10):1364–1375.

Higgins, A. (1991). North Greenland Glacier Velocities and Calf Ice Production. *Polarforschung*, 60(1):1–23.

Holland, D., Thomas, R., de Young, B., Ribergaard, M., and Lyberth, B. (2008). Acceleration of Jakobshavn Isbrae triggered by warm subsurface ocean waters. *Nature Geoscience*, 1(10):659–664.

Hooke, R. (1981). Flow Law for Polycrystalline Ice in Glaciers: Comparison of Theoretical Predictions, Laboratory Data, and Field Measurements. *Reviews of Geophysics and Space Physics*, 19(4):664–672.

Hooke, R. and Pohjola, V. (1994). Hydrology of a segment of a glacier situated in an overdeepening, Storglaciaren, Sweden. *Journal of Glaciology*, 40(134):140–148.

Howat, I., Joughin, I., Fahnestock, M., Smith, B., and Scambos, T. A. (2008). Synchronous retreat and acceleration of southeast Greenland outlet glaciers 2000-06: ice dynamics and coupling to climate. *Journal of Glaciology*, 54(187):646–660.

Howat, I., Negrete, A., and Smith, B. (2014). The Greenland Ice Mapping Project (GIMP) land classification and surface elevation datasets. *The Cryosphere Discuss*, 8:453–478.

Hutchinson, M. (1988). Calculation of hydrologically sound digital elevation models. In *Proceedings of the Third International Symposium on Spatial Data Handling, Sydney*, Columbus, Ohio. International Geographical Union.

Hutchinson, M. (1989). A new procedure for gridding elevation and stream line data with automatic removal of spurious pits. *Journal of Hydrology*, 106(3-4):211–232.

Iken, A. (1981). The effect of subglacial water pressure on the sliding velocity of a glacier in an idealised numerical model. *Journal of Glaciology*, 27(97):407–421.

Iverson, N., Cohen, D., Hooyer, T., Fischer, U., Jackson, M., Moore, P., Lappegard, G., and Kohler, J. (2003). Effects of Basal Debris on Glacier Flow. *Science*, 301(5629):81–84.

Jacka, T. (1984). Laboratory studies on relationships between ice crystal size and flow rate. *Cold Regions Science and Technology*, 10(1):261–268.

Jezek, K., Wu, X., Gogineni, P., Rodriguez, E., Freeman, A., Rodriguez-Morales, F., and Clark, C. (2011). Radar images of the bed of the Greenland Ice Sheet. *Geophysical Research Letters*, 38(1):1–5.

Johnsen, S., Dahl-Jensen, D., Dansgaard, W., and Gundestrup, N. (1995). Greenland palaeotemperature derived from GRIP borehole temperatue and ice core isotope profiles. *Tellus*, 47(5):624–629.

Jones, S. and Glen, J. (1969). The effect of dissolved impurities on the mechanical properties of ice crystals. *Philosophical Magazine*, 19(157):13–24.

Joughin, I. (2002). Ice-sheet velocity mapping: a combined interferometric and speckle-tracking approach. *Annals of Glaciology*, 34(1):195–201.

Joughin, I., Abdalati, W., and Fahnestock, M. (2004). Large fluctuations in speed on Greenland's Jakobshavn Isbrae glacier. *Nature*, 432(7017):608–610.

Joughin, I., Fahnestock, M., Kwok, R., Gogineni, S. P., and Allen, C. (1999). Ice flow of Humboldt, Petermann and Ryder Gletscher, northern Greenland. *Journal of Glaciology*, 45(150):231–241.

Joughin, I., Smith, B., Howat, I., Scambos, T. A., and Moon, T. (2010). Greenland flow variability from ice-sheet-wide velocity mapping. *Journal of Glaciology*, 56(197):415–430.

Kamb, B. (1970). Sliding motion of glaciers: theory and observation. *Reviews of Geophysics and Space Physics*, 8(4):673–728.

Kamb, B. (1991). Rheological Nonlinearity and Flow Instability in the Deforming Bed Mechanism of Ice Stream Motion. *Journal of Geophysical Research: Solid Earth*, 96(B10):16585–16595.

Kessler, M., Anderson, R., and Briner, J. (2008). Fjord insertion into continental margins driven by topographic steering of ice. *Nature Geoscience*, 1(6):365–369.

Krabill, W., Hanna, E., Huybrechts, P., Abdalati, W., Cappelen, J., Csatho, B., Frederick, E., Manizade, S., Martin, C., Sonntag, J., Swift, R., Thomas, R., and Yungel, J. (2004). Greenland Ice Sheet: Increased coastal thinning. *Geophysical Research Letters*, 31(24):1–4.

Layberry, R. and Bamber, J. L. (2001). A new ice thickness and bed data set for the Greenland ice sheet: 2. Relationship between dynamics and basal topography. *Journal of Geophysical Research: Atmospheres*, 106(D24):33781–33788.

Li, J., Paden, J., Leuschen, C., Rodriguez-Morales, F., Hale, R., Arnold, E., Crowe, R., Gomez-Garcia, D., and Gogineni, P. (2013). High-Altitude Radar Measurements of Ice Thickness Over the Antarctic and Greenland Ice Sheets as a Part of Operation IceBridge. *IEEE Transactions on Geoscience and Remote Sensing*, 51(2):742–754.

Lliboutry, L. (1959). Une theorie du frottement du glacier sur son lit. *Annales de Geophysique*, 15(2):250–265.

MacAyeal, D. (1993). A tutorial on the use of control methods in ice-sheet modelling. *Journal of Glaciology*, 39(131):91–98.

Marshall, S. (2005). Recent advances in understanding ice sheet dynamics. *Earth and Planetary Science Letters*, 240(2):191–204.

McIntyre, N. (1985). The Dynamics of Ice-Sheet Outlets. *Journal of Glaciology*, 31(108):99–107.

McNabb, R., Hock, R., O'Neel, S., Ramussen, L., Ahn, Y., Braun, M., Conway, H., Herreid, S., Joughin, I., Pfeffer, W., Smith, B., and Truffer, M. (2012). Using surface velocities to calculate ice thickness and bed topography: a case study at Columbia Glacier, Alaska, USA. *Journal of Glaciology*, 58(212):1151–1164.

Meier, M., Lundstrom, S., Stone, D., Kamb, B., Engelhardt, H., Humphrey, N., Dunlap, W., Fahnestock, M., Krimmel, R., and Walters, R. (1994). Mechanical and hydrologic basis for the rapid motion of a large tidewater glacier. *Journal of Geophysical Research: Solid Earth*, 99(B8):15219–15229.

Meier, M. and Post, A. (1987). Fast Tidewater Glaciers. *Journal of Geophysical Research: Solid Earth*, 92(B9):9051–9058.

Moon, T., Joughin, I., Smith, B., and Howat, I. (2012). 21st-Century Evolution of Greenland Outlet Glacier Velocities. *Science*, 336(6081):576–578.

Morlighem, M., Rignot, E., Mouginot, J., Seroussi, H., and Larour, E. (2014). Deeply incised submarine glacial valleys beneath the Greenland ice sheet. *Nature Geoscience*, AOP:1–5.

Morlighem, M., Rignot, E., Mouginot, J., Wu, X., Seroussi, H., Larour, E., and Paden, J. (2013). High-resolution bed topography mapping of Russell Glacier, Greenland, inferred from Operation Icebridge. *Journal of Glaciology*, 59(218):1015–1023.

Morlighem, M., Rignot, E., Seroussi, H., Larour, E., Ben Dhia, H., and Aubry, D. (2010). Spatial patterns of basal drag inferred using control methods from a full-Stokes and simpler models for Pine Island Glacier, Antarctica. *Geophysical Research Letters*, 37(14):1–6.

Morlighem, M., Rignot, E., Seroussi, H., Larour, E., Ben Dhia, H., and Aubry, D. (2011). A mass conservation approach for mapping glacier ice thickness. *Geophysical Research Letters*, 38(19):1–6.

Nick, F. (2006). *Modelling the behavior of tidewater glaciers*. PhD thesis, Utrecht University.

Nick, F., Luckman, A., Vieli, A., van der Veen, C., van As, D., van de Wal, R., Pattyn, F., Hubbard, A., and Floricioiu, D. (2010). The response of Petermann Glacier, Greenland, to large calving events, and its future stability in the context of atmospheric and oceanic warming. *Journal of Glaciology*, 58(208):229–239.

Nick, F., Vieli, A., Howat, I., and Joughin, I. (2009). Large-scale changes in Greenland outlet glacier dynamics triggered at the terminus. *Nature Geoscience*, 2(2):110–114.

Nye, J. (1957). The Distribution of Stress and Velocity in Glaciers and Ice-Sheets. *Proceedings of the Royal Society A*, 239(1216):113–133.

O'Leary, M. and Christoffersen, P. (2013). Calving on tidewater glaciers amplified by submarine frontal melting. *The Cryosphere*, 7:119–128.

O'Neel, S., Echelmeyer, K., and Motyka, R. (2003). Short-term variations in calving of a tidewater glacier: LeConte Glacier, Alaska, USA. *Journal of Glaciology*, 49(167):587–598.

O'Neel, S., Pfeffer, W., Krimmel, R., and Meier, M. (2005). Evolving force balance at Columbia Glacier, Alaska, during its rapid retreat. *Journal of Geophysical Research: Earth Surface*, 110(F3):1–18.

Palmer, S., Dowdeswell, J. A., Christoffersen, P., Young, D., Blankenship, D., Greenbaum, J., Benham, T., Bamber, J. L., and Siegert, M. (2013). Greenland subglacial lakes detected by radar. *Geophysical Research Letters*, 40(23):6154–6159.

Pelto, M. and Warren, C. (1991). Relationship between tidewater glacier calving velocity and water depth at the calving front. *Annals of Glaciology*, 15:115–118.

Peters, M., Blankenship, D., Carter, S., Kempf, S., Young, D., and Holt, J. (2007). Along-Track Focusing of Airborne Radar Sounding Data from West Antarctica for Improved Basal Reflection Analysis and Layer Detection. *IEEE Transactions on Geoscience and Remote Sensing*, 45(9):2725–2736.

Peters, M., Blankenship, D., and Morse, D. (2005). Analysis techniques for coherent airborne radar sounding: Application to West Antarctic Ice Streams. *Journal of Geophysical Research: Solid Earth*, 110(B6):1–17.

Petra, N., Zhu, H., Stadler, G., Hughes, T., and Ghattas, O. (2012). An inexact Gauss-Newton method for inverison of basal sliding and rheology parameters in a nonlinear Stokes ice sheet model. *Journal of Glaciology*, 58(211):889–903.

Pritchard, H. D., Arthern, R., Vaughan, D., and Edwards, L. (2009). Extensive dynamic thinning on the margins of the Greenland and Antarctic ice sheets. *Nature*, 461(7266):971–975.

Rasmussen, L. (1985). Adjusting two-dimensional velocity data to obey continuity. *Journal of Glaciology*, 31(108):115–119.

Rasmussen, L. (1988). Bed Topography and Mass-Balance Distribution of Columbia Glacier, Alaska, USA, Determined from Sequential Aerial Photography. *Journal of Glaciology*, 34(117):208–216.

Reeh, N., Mayer, C., Miller, H., Thomsen, H., and Weidick, A. (1999). Present and past climate control on fjord glaciations in Greenland: Implications for IRD-deposition in the sea. *Geophysical Research Letters*, 26(8):1039–1042.

Reeh, N. and Olesen, O. (1986). Velocity measurements on Daugaard-Jensen Gletscher, Scoresby Sund, East Greenland. *Annals of Glaciology*, 8:146–150.

Rignot, E., Gogineni, S. P., Joughin, I., and Krabill, W. (2001). Contribution to the glaciology of northern Greenland from satellite radar interferometry. *Journal of Geophysical Research: Atmospheres*, 106(D24):34007–34019.

Rignot, E., Gogineni, S. P., Krabill, W., and Ekholm, S. (1997). North and Northeast Greenland Ice Discharge from Satellite Radar Interferometry. *Science*, 276(5314):934–937.

Rignot, E. and Kanagaratnam, P. (2006). Changes in the Velocity Structure of the Greenland Ice Sheet. *Science*, 311(5763):986–990.

Rignot, E., Koppes, M., and Velicogna, I. (2010). Rapid submarine melting of the calving faces of West Greenland glaciers. *Nature Geoscience*, 3(3):187–191.

Rignot, E., Velicogna, I., van den Broeke, M. R., Monaghan, A., and Lenaerts, J. T. M. (2011). Acceleration of the contribution of the Greenland and Antarctic ice sheets to sea level rise. *Geophysical Research Letters*, 38(5):1–5.

Rutt, I., Hagdorn, M., Hulton, N., and Payne, A. J. (2009). The Glimmer community ice sheet model. *Journal of Geophysical Research: Earth Surface*, 114(F2):1–22.

Scambos, T. A., Fricker, H., Liu, C.-C., Bohlander, J., Fastook, J., Sargent, A., Massom, R., and Wu, A.-M. (2009). Ice shelf disintegration by plate bending and hydro-fracture: Satellite observations and model results of the 2008 Wilkins ice shelf break-ups. *Earth and Planetary Science Letters*, 280(1-4):51–60.

Scambos, T. A. and Haran, T. (2002). An image-enhanced DEM of the Greenland ice sheet. *Annals of Glaciology*, 34(1):291–298.

Scambos, T. A., Hulbe, C., Fahnestock, M., and Bohlander, J. (2000). The link between climate warming and break-up of ice shelves in the Antarctic Peninsula. *Journal of Glaciology*, 46(154):516–530.

Schoof, C. (2002). Basal perturbations under ice streams: form drag and surface expression. *Journal of Glaciology*, 48(162):407–416.

Schoof, C. (2005). The effect of cavitation on glacier sliding. *Proceedings of the Royal Society A*, 461(2055):609–627.

Schoof, C. (2010). Ice-sheet acceleration driven by melt supply variability. *Nature*, 468(7325):803–806.

Seale, A., Christoffersen, P., Mugford, R., and O'Leary, M. (2011). Ocean forcing of the Greenland Ice Sheet: Calving fronts and patterns of retreat identified by automatic satellite monitoring of eastern outlet glaciers. *Journal of Geophysical Research: Earth Surface*, 116(F3):1–16.

Seddik, H., Greve, R., Zwinger, T., Gillet-Chaulet, F., and Gagliardini, O. (2012). Simulations of the Greenland ice sheet 100 years into the future with the full Stokes model Elmer/Ice. *Journal of Glaciology*, 58(209):427–440.

Seroussi, H., Morlighem, M., Rignot, E., Larour, E., Aubry, D., Ben Dhia, H., and Kristensen, S. (2011). Ice flux divergence anomalies on 79north Glacier, Greenland. *Geophysical Research Letters*, 38(9):1–5.

Shepherd, A., Ivins, E. R., Geruo, A., Barletta, V. R., Bentley, M. J., Bettadpur, S., Briggs, K. H., Bromwich, D. H., Forsberg, R., Galin, N., Horwath, M., Jacobs, S., Joughin, I., King, M. A., Lenaerts, J. T. M., Li, J., Ligtenberg,

S. R. M., Luckman, A., Luthcke, S. B., McMillan, M., Meister, R., Milne, G., Mouginot, J., Muir, A., Nicolas, J. P., Paden, J., Payne, A. J., Pritchard, H., Rignot, E., Rott, H., Sørensen, L. S., Scambos, T. A., Scheuchl, B., Schrama, E. J. O., Smith, B., Sundal, A. V., van Angelen, J. H., van de Berg, W. J., van den Broeke, M. R., Vaughan, D. G., Velicogna, I., Wahr, J., Whitehouse, P. L., Wingham, D. J., Yi, D., Young, D., and Zwally, H. J. (2012). A Reconciled Estimate of Ice Sheet Mass Balance. *Science*, 338(6111):1183–1189.

Siegert, M., Dowdeswell, J. A., Gorman, M., and McIntyre, N. (1996). An inventory of Antarctic sub-glacial lakes. *Antarctic Science*, 8(3):281–286.

Stearns, L. (2011). Dynamics and mass balance of four large East Antarctic outlet glaciers. *Annals of Glaciology*, 52(59):116–126.

Stearns, L., Hamilton, G., and Reeh, N. (2005). Multi-decadal record of ice dynamics on Daugaard Jensen Gletscher, East Greenland, from satellite imagery and terrestrial measurements. *Annals of Glaciology*, 42(1):53–58.

Steffen, K. and Box, J. (2001). Surface climatology of the Greenland ice sheet: Greenland Climate Network 1995-1999. *Journal of Geophysical Research: Atmospheres*, 106(D24):33951–33964.

Swift, D., Nienow, P., Spedding, N., and Hoey, T. (2002). Geomorphic implications of subglacial drainage configuration: rates of basal sediment evacuation controlled by seasonal drainage system evolution. *Sedimentary Geology*, 149(1-3):5–19.

Swift, D., Persano, C., Stuart, F., Gallagher, K., and Whitham, A. (2008). A reassessment of the role of ice sheet glaciation in the long-term evolution of the East Greenland fjord region. *Geomorphology*, 97(1-2):109–125.

Tulaczyk, S., Kamb, B., and Engelhardt, H. (2000). Basal mechanics of Ice Stream B, West Antarctica. 1. Till mechanics. *Journal of Geophysical Research: Solid Earth*, 105(B1):463–481.

van den Broeke, M. R., Bamber, J. L., Ettema, J., Rignot, E., Schrama, E. J. O., van de Berg, W. J., van Meijgaard, E., Velicogna, I., and Wouters, B. (2009). Partitioning Recent Greenland Mass Loss. *Science*, 326(5955):984–986.

van der Veen, C. (2002). Calving Glaciers. *Progress in Physical Geography*, 26(1):96–122.

van der Veen, C. and Whillans, I. (1989). Force budget: I. theory and numerical methods. *Journal of Glaciology*, 35(119):53–60.

van Meijgaard, E., van Ulft, L., van de Berg, W. J., Bosveld, F., van den Hurk, B., Lenderink, G., and Siebesma, A. (2008). The KNMI regional atmospheric climate model RACMO version 2.1. KNMI Tech Report 302, Royal Netherlands Meteorological Institute (KNMI).

Vaughan, D., Comiso, J., Allison, I., Carrasco, J., Kaser, G., Kwok, R., Mote, P., Murray, T., Paul, F., Ren, J., Rignot, E., Solomina, O., Steffen, K., and Zhang, T. (2013). *Climate Change 2013: The Physical Science Basis. Contribution of Working Group I to the Fifth Assessment Report of the Intergovernmental Panel on Climate Change*, chapter Observations: Cryosphere. Cambridge University Press: Cambridge, UK.

Vieli, A. and Payne, A. J. (2003). Application of control methods for modelling the flow of Pine Island Glacier, West Antarctica. *Annals of Glaciology*, 36(1):197–204.

Walsh, K., Howat, I., Ahn, Y., and Enderlin, E. (2012). Changes in the marine-terminating outlet glaciers of central-east Greenland, 2000-2010. *The Cryosphere*, 6:211–220.

Weertman, J. (1957). On the Sliding of Glaciers. *Journal of Glaciology*, 3(21):33–38.

Weertman, J. (1964). The theory of glacier sliding. *Journal of Glaciology*, 5(39):287–303.

Weertman, J. (1967). Sliding of Nontemperate Glaciers. *Journal of Geophysical Research*, 72(2):521–523.

Weertman, J. (1983). Creep Deformation of Ice. *Annual Reviews of Earth and Planetary Science*, 11:215–240.

Young, D., Wright, A., Roberts, J., Warner, R., Young, N., Greenbaum, J., Schroeder, D., Holt, J., Sugden, D., Blankenship, D., van Ommen, T., and Siegert, M. (2011). A dynamic early East Antarctic Ice Sheet suggested by ice-covered fjord landscapes. *Nature*, 474(7349):72–75.

Zwally, H. J., Abdalati, W., Herring, T., Larson, K., Saba, J., and Steffen, K. (2002). Surface Melt-Induced Acceleration of Greenland Ice-Sheet Flow. *Science*, 297(5579):218–222.